

2020-09-30

# Grainenergy release governs mobility of debris flow due to solidliquid mass release

Cao, Zhixian

<http://hdl.handle.net/10026.1/17651>

---

10.1002/esp.4939

Earth Surface Processes and Landforms

Wiley

---

*All content in PEARL is protected by copyright law. Author manuscripts are made available in accordance with publisher policies. Please cite only the published version using the details provided on the item record or document. In the absence of an open licence (e.g. Creative Commons), permissions for further reuse of content should be sought from the publisher or author.*

1           **Grain-energy release governs mobility of debris flow due to**  
2                                   **solid-liquid mass release**

3           Zhixian Cao <sup>1\*</sup>, Ji Li<sup>1, 2</sup>, Alistair Borthwick<sup>3</sup>, Qingquan Liu<sup>4\*\*</sup>, Gareth Pender<sup>5</sup>

4  
5   <sup>1</sup> State Key Laboratory of Water Resources and Hydropower Engineering Science,  
6   Wuhan University, Wuhan, China;

7   <sup>2</sup> Zienkiewicz Centre for Computational Engineering, College of Engineering,  
8   Swansea University, Swansea, UK;

9   <sup>3</sup> Institute for Infrastructure and Environment, The University of Edinburgh, Edinburgh,  
10   UK;

11   <sup>4</sup> Department of Mechanics, Beijing Institute of Technology, Beijing, China;

12   <sup>5</sup> Institute for Infrastructure and Environment, Heriot-Watt University, Edinburgh, UK.

13  
14   **Correspondence**

15   Zhixian Cao, State Key Laboratory of Water Resources and Hydropower Engineering  
16   Science, Wuhan University, Wuhan 430072, China.

17   Email: [zxcao@whu.edu.cn](mailto:zxcao@whu.edu.cn)

18  
19   Qingquan Liu, Department of Mechanics, Beijing Institute of Technology, Beijing,  
20   100081, China

21   Email: [liuqq@bit.edu.cn](mailto:liuqq@bit.edu.cn)

24 **ABSTRACT**

25 Debris flows often exhibit high mobility, leading to extensive hazards far from their  
26 sources. Although it is known that debris flow mobility increases with initial volume,  
27 the underlying mechanism remains uncertain. Here, we reconstruct the  
28 mobility-volume relation for debris flows using a recent depth-averaged two-phase  
29 flow model without evoking reduced friction coefficient, challenging currently  
30 prevailing friction-reduction hypotheses. Physical experimental debris flows driven by  
31 solid-liquid mass release and extended numerical cases at both laboratory and field  
32 scales are resolved by the model. For the first time, we probe into the energetics of  
33 the debris flows and find that, whilst the energy balance holds and fine and coarse  
34 grains play distinct roles in debris flow energetics, the grains as a whole release  
35 energy to the liquid due to inter-phase and inter-grain size interactions, and this  
36 grain-energy release correlates closely with mobility. Despite uncertainty arising from  
37 the model closures, our results provide insight into the fundamental mechanisms  
38 operating in debris flows. We propose that debris flow mobility is governed by  
39 grain-energy release, thereby facilitating a bridge between mobility and internal  
40 energy transfer. Initial volume of debris flow is inadequate for characterizing debris  
41 flow mobility, and a friction-reduction mechanism is not a prerequisite for the high  
42 mobility of debris flows. By contrast, inter-phase and inter-grain size interactions play  
43 primary roles and should be incorporated explicitly in debris flow models. Our findings  
44 are qualitatively encouraging and physically meaningful, providing implications not  
45 only for assessing future debris flow hazards and informing mitigation and adaptation  
46 strategies, but also for unravelling a spectrum of earth surface processes including  
47 heavily sediment-laden floods, subaqueous debris flows and turbidity currents in  
48 rivers, reservoirs, estuaries and ocean.

49 **KEYWORDS:** debris flows; solid-liquid mass release; high mobility; mobility-volume  
50 relation; energy transfer; grain-energy release

51

## 52 **1 INTRODUCTION**

53 Debris flows form when masses of poorly sorted sediments, agitated and saturated by  
54 water, surge down steep slopes in response to gravitational effects, and can grow  
55 dramatically in speed and size by entraining materials from beds and banks (Iverson,  
56 1997). The severity of these hazards is largely dependent on the speed and travel  
57 distance, which are collectively described as “mobility” (Iverson et al., 2015). Owing to  
58 their destructive power, debris flows can produce significant natural hazards. Often,  
59 debris flows generated by solid-liquid mass releases exhibit exceptionally high  
60 mobility leading to catastrophic disasters extending far beyond the source zone  
61 (Iverson, 1997; Legros, 2002; Rickenmann, 2005; Lucas, Mangeney, & Ampuero,  
62 2014; Gregoretto, Degetto, Bernard, & Boreggio, 2018; Chen, Liu, Wang, Zao, & Zhou,  
63 2019). Field observations and experimental measurements indicate that debris flow  
64 mobility increases with initial volume (Iverson, 1997; Rickenmann, 2005), and is  
65 further enhanced by bed erosion, water content, and grain-size heterogeneity  
66 (Iverson, 1997; Legros, 2002; Rickenmann, 2005). Several empirical relationships  
67 have been proposed to estimate debris flow mobility on the basis of initial volume  
68 alone (e.g., Corominas, 1996; Rickmann, 1999, 2005). Field data also reveal that for  
69 a given volume, debris flows, as typical liquid-solid two-phase flows, exhibit much  
70 higher efficiency than avalanches and rock falls (Hayashi & Self, 1992; Iverson, 1997;  
71 Vallance & Scott, 1997; Legros, 2002), which behave physically as single-phase  
72 granular flows. Usually, the mobility of debris flow is characterized by the horizontal  
73 run-out distance  $L$  or efficiency  $e$  ( $=L/H$  where  $H$  is the vertical fall height)  
74 (Iverson, 1997; Legros, 2002; Lucas et al., 2014; Rickenmann, 2005). In particular, for  
75 extremely large volume events, the efficiency of non-channelized natural debris flow

76 can reach up to 25 (Iverson, 1997). Debris flows can also be generated by run-off  
77 (e.g., Kean, McCoy, Tucker, Staley, & Coe, 2013; Hürlimann, Abanco, Moya, &  
78 Vilajosana, 2014; Ma, Deng, & Wang, 2018), in which case mobility is mainly  
79 controlled by the triggering discharge (Lanzoni, Gregoretti, & Stancanelli, 2017). The  
80 present study focuses on debris flow due to solid-liquid mass release.

81 However, the mechanisms underlying the high mobility of debris flows due to  
82 solid-liquid mass release remain poorly understood (Iverson, 1997; Lucas et al.,  
83 2014). Many fundamentally distinct friction-reduction hypotheses have been  
84 proposed to explain the high mobility of general geophysical mass flows (e.g.,  
85 avalanches, rock falls and debris flows), including those based on velocity-dependent  
86 friction weakening (Lucas et al., 2014), fluidization by water (Legros, 2002; Pudasaini  
87 & Miller, 2013), entrainment (Hung & Evans, 2004; Mangeney, Tsimring, Volfson,  
88 Aranson, & Bouchut, 2007; Lube et al., 2012), pore fluid pressure (Iverson et al., 2011;  
89 Iverson et al., 2015), grain-size distribution (de Haas, Braat, Leuven, Lokhorst, &  
90 Kleinhans, 2015; Kaitna, Palucis, Yohannes, Hill, & Dietrich, 2016), grain  
91 segregation-induced momentum advection (Johnson et al., 2012) or friction decrease  
92 (Linares-Guerrero, Goujon, & Zenit, 2007), flash friction heating (Goren & Aharonov,  
93 2007; Singer, McKinnon, Schenk, & Moore, 2012; Wang, Dong, & Cheng, 2017),  
94 dynamic fragmentation (Perinotto et al., 2015), acoustic fluidization (Johnson et al.,  
95 2016), and an air cushion trapped underneath a moving mass (Shreve, 1968).  
96 Although certain mechanisms may be appropriate for particular site-specific events,  
97 none of these hypotheses provides a universal explanation for the high mobility of  
98 debris flows (Lucas et al., 2014; Iverson, 2016), which essentially incorporate diverse  
99 complicated physical processes (Lucas et al., 2014), including inter-phase  
100 interactions between water and sediments, multiple grain sizes, and substantial mass

101 exchange with the bed. Furthermore, the relation between mobility and initial volume  
102 cannot be properly reconstructed without using reduced friction coefficients (Lucas et  
103 al., 2014; Johnson et al., 2016) with much lower values than generally accepted for  
104 geological materials (Singer et al., 2012). Actually, most friction-reduction hypotheses  
105 are necessarily rooted in conjecture rather than fact (Iverson, 2016) because hardly  
106 any experimental evidence is available for validation purposes (Utili, Zhao, & Houlby,  
107 2015; Iverson, 2016). Also, none of these hypotheses is able to fully resolve debris  
108 flow dynamics because of the underlying assumptions concerning single-phase dry  
109 granular flow without water (Shreve, 1968; Hungr and Evans, 2004; Linares-Guerrero  
110 et al., 2007; Mangeney et al., 2007; Lucas et al., 2014; Johnson et al., 2016), single  
111 (uniform) grain size (Shreve, 1968; Hungr & Evans, 2004; Mangeney et al., 2007;  
112 Goren et al., 2007; Lucas et al., 2014; Johnson et al., 2016), and negligible mass  
113 exchange with the bed (Shreve, 1968; Goren et al., 2007; Lucas et al., 2014; Johnson  
114 et al., 2016).

115 Computational modelling holds great promise for resolving the mechanisms behind  
116 the high mobility of debris flows. The past several decades have witnessed the  
117 development and application of many numerical models of debris flows, the majority  
118 being based on depth-averaged single-phase flow formulations (e.g., Takahashi,  
119 Nakagawa, Harada, & Yamashiki, 1992; Iverson, 1997; McDougall & Hungr, 2005;  
120 Medina, Hürlimann, & Bateman, 2008; Armanini, 2009; Rosatti & Begnudelli, 2013;  
121 Iverson & George, 2014; Lucas et al., 2014; Frank, McArdell, Huggel, & Vieli, 2015;  
122 Cuomo, Pastor, Capobianco, & Cascini, 2016; Xia, Li, Cao, Liu, & Hu, 2018; Federico  
123 & Cesali, 2019; Gregoretto et al., 2019). Notably, a single-phase flow model based on  
124 energy conservation was proposed by Wang, Morgenstern, & Chan (2010). In  
125 general however, only the velocity of water-sediment mixture is solved in these

126 models, and the relative motions and interactions between the water and sediment  
127 phases are not explicitly incorporated, even though both are primary features of  
128 debris flows (e.g., Iverson, 1997; Pudasaini, 2012). In this connection, two-phase flow  
129 theory is certainly the way forward (Armanini, 2013), whereby water and sediment  
130 phases are separately resolved according to their respective mass and momentum  
131 conservation laws. Indeed, depth-averaged two-phase flow models are not new in  
132 debris flow modelling (e.g., Pitman & Le, 2005; Pelanti, Bouchut, & Mangeney, 2008;  
133 Pailha & Pouliquen, 2009; Pudasaini, 2012; Kowalski & McElwaine, 2013; Bouchut,  
134 Fernandez-Nieto, Mangeney, & Narbona-Reina, 2015). However, previous two-phase  
135 flow models have suffered from several major shortcomings. First, they are confined  
136 to single-sized sediment transport. In practice, sediments in debris flows may be  
137 heterogeneous with widely distributed sizes, ranging from clay (particle diameter  
138  $\approx 10^{-5}$  m) to boulders (particle diameter  $\approx 10^1$  m) (Iverson, 1997). Grain size data  
139 reveal the oversimplification of debris flow models that presume the sediment mixture  
140 comprises particles of a single grain size, and they also reinforce the notion that  
141 multiple grain sizes may be critical to debris flow dynamics (Iverson, 1997). Second,  
142 existing depth-averaged two-phase flow models have exclusively ignored mass  
143 exchange between the flow and the bed, a vital physical aspect of debris flows.  
144 Inevitably, they are restricted to modeling debris flows over fixed beds. Third, existing  
145 two-phase flow models have generally neglected the effects of liquid and solid  
146 fluctuations. Notably, inclusion of stresses due to liquid and solid fluctuations has  
147 been demonstrated to be important in reproducing debris flow kinetics (Li, Cao, Hu,  
148 Pender, & Liu, 2018b).

149 Here, we apply a recently developed numerical depth-averaged two-phase flow  
150 model (Li, Cao, Hu, Pender, & Liu, 2018a) to reproduce the full sets of USGS

151 experimental debris flows reported by Iverson et al. (2011) and then resolve a  
152 spectrum of laboratory- and field-scale numerical cases designed according to the  
153 USGS experiments. Unlike previous numerical models based on reduced friction  
154 coefficients (Lucas et al., 2014), the friction coefficients used here have values within  
155 the conventional ranges. We then probe into the energetics of debris flows by  
156 evaluating the energy components and energy changes of both the liquid and solid  
157 phases for all the aforementioned experimental and numerical cases. Energy transfer  
158 within debris flow is linked with its mobility. This, the first work of its kind, is certainly  
159 warranted given that debris flow mobility has perplexed scientists for decades.

160 The present work aims to enhance the understanding of debris flow mobility based on  
161 numerical solutions from a two-phase flow model (Li et al., 2018a). The model has  
162 incorporated as much physics as possible to expand capability and minimize  
163 uncertainty, and has been validated against all available observed data from USGS  
164 experiments (Iverson, Logan, LaHusen, & Berti, 2010; Iverson et al., 2011). In  
165 particular, it features a physical step forward in debris flow modelling by incorporating  
166 inter-phase and inter-grain size interactions, multiple grain sizes, mass exchange with  
167 the bed and strong liquid and solid fluctuations. Yet, like other numerical models for  
168 general earth surface flows, a set of relationships has to be introduced to close the  
169 model, and quantitatively some degree of uncertainty is inevitable. In particular, the  
170 closure models for inter-grain size interaction, liquid and solid fluctuations, and mass  
171 exchange with the bed are tentatively employed for modelling debris flow, given that  
172 no generally valid closure models have been forthcoming to date. Although the  
173 closure models remain imperfect, the modelling results provide some insight into the  
174 fundamental mechanisms operating in debris flows.



175

## 176 **2 METHODS**

### 177 **2.1 Case descriptions**

#### 178 **2.1.1 USGS debris flow experiments**

179 A series of laboratory-scale experiments was conducted at the USGS debris-flow  
180 flume (Iverson, 1997; Iverson et al., 2011). The experiments involved unsteady,  
181 non-uniform debris flows from initiation to deposition. The USGS debris-flow flume  
182 comprised a straight rectangular concrete channel, 95 m long, 2 m wide, and 1.2 m  
183 deep (Figure 1), connected to an adjacent runout pad. A 2 m high vertical headgate  
184 was used to retain static debris prior to its release. For  $0 \leq x \leq 74$  m, the flume bed  
185 had uniform slope,  $\theta = 31^\circ$ , whereas for  $x > 74$  m, the bed slope tended towards  
186 horizontal. Approximately  $6 \text{ m}^3$  of a water-saturated sediment mixture called SGM, of  
187 porosity  $p = 0.49$  (corresponding to water content  $\theta_f = p = 0.49$ ), and composed of  
188 about 53% gravel, 37% sand, and 7% mud-sized grains with standard deviation  $\sigma =$   
189 8.87, was released abruptly from a headgate and propagated downslope. Table S1  
190 lists the detailed sediment composition of SGM. Here two typical experimental cases  
191 are revisited. For the erodible-bed experiment (labelled “EXP-E”), bed sediment of  
192 unsaturated SGM with water content  $\theta_f = 0.28$ , volume  $10.9 \text{ m}^3$ , thickness  $\sim 12$  cm  
193 initially covered the uniformly sloping ramp from  $x = 6$  m to 53 m. For the fixed-bed  
194 experiment (labelled “EXP-F”), the debris flow was released in the absence of bed  
195 sediment. Table S2 in Supporting Information lists details of the experimental cases.

196

197

198 **FIGURE 1** Flume geometry for USGS debris flow experiments [from Iverson et al.  
199 (2011)].

200

## 201 **2.1.2 Laboratory-scale numerical cases**

202 Using numerical simulation, we extend the parameter ranges covered in the USGS  
203 experiments to investigate the influence of initial debris flow volume. Also, the effects  
204 of bed erosion, water content, and grain-size heterogeneity are investigated (Table  
205 S3). Furthermore, a similar channel with the same length  $L_0$  as that used in USGS  
206 experiments but different sloping angle ( $\theta = 40^\circ$ ) is used (Figure 2a). We classify the  
207 case studies into fixed-bed and erodible-bed studies; therefore, laboratory-scale  
208 numerical cases are labelled “FBS” and “EBS”. Briefly, the initial volume of the  
209 released debris flow, which is composed of a water-saturated sediment mixture SGM,  
210 ranges from  $1 \text{ m}^3$  to  $1600 \text{ m}^3$  in order to investigate the volume effect. Then, for each  
211 debris flow (volume varying from  $6 \text{ m}^3$  to  $1600 \text{ m}^3$ ), the bed sediment, which is the  
212 same as that used in USGS experiment, is placed on the sloping ramp to study the  
213 effect of bed erosion (i.e., EBS cases). To investigate the effect of water content, the  
214 initial water content  $\theta_f$  of the released debris flow is reduced from 0.49 to 0.3 or 0.1,  
215 and to address the effect of heterogeneity, the grain-size heterogeneity is adjusted by  
216 altering the standard deviation of sediment composition (i.e.,  $\sigma$  was set to 13.17 or  
217 4.25), while retaining the same median size  $d_{50}$  ( $= 3.22 \text{ mm}$ , the particle size at which

218 50% of the sediments are finer). Except for the initial values of flow thickness, water  
219 content and sediment composition of the released debris flow, and bed elevation (see  
220 Table S3 in Supporting Information), all other parameters are kept the same as in the  
221 experiments.

222

### 223 **2.1.3 Field-scale numerical cases**

224 The field-scale numerical case studies are qualitatively similar to the laboratory-scale  
225 cases described above. The computational domain has an upstream ramp of uniform  
226 inclination angle of  $\theta = 31^\circ$  or  $40^\circ$ , length  $L_0$  and height  $H_0$ , which joins (at its  
227 downstream end) a horizontal runout pad (Figure 2b). For intermediate field-scale  
228 cases (labelled “FBM” and “EBM”), the length  $L_0$  and width  $B$  of the sloping  
229 channel are respectively 400 m and 20 m, whereas for large field-scale cases  
230 (labelled “FBL” and “EBL”), the corresponding length  $L_0$  and width  $B$  are 1600 m  
231 and 50 m, respectively. First, the effect of initial debris flow volume is investigated.  
232 For the intermediate field-scale cases, the initial volume of debris flow ranges from 30  
233  $\text{m}^3$  to  $1.2 \times 10^7 \text{ m}^3$ , whereas for the large field-scale cases, the initial volume varies  
234 from  $1000 \text{ m}^3$  to  $10^9 \text{ m}^3$ . The released debris flow is composed of a water-saturated  
235 sediment mixture SGM (i.e.,  $\theta_f = 0.49$  and  $\sigma = 8.87$ ), which is the same as in the  
236 USGS experiments. Then the effects of bed erosion, water content, and grain-size  
237 heterogeneity are studied. In particular, to investigate the effect of bed erosion, for  
238 EBM cases, the unsaturated bed sediment SGM ( $\theta_f = 0.28$ ) of volume  $V_b = 1500$   
239  $\text{m}^3$  covers the sloping ramp, whereas for EBL cases, that of volume  $V_b = 10^5 \text{ m}^3$  is  
240 placed on the sloping ramp. To address the respective effects of water content and

241 grain-size heterogeneity, for both FBM and FBL cases, we consider reduced water  
242 content (i.e.,  $\theta_f = 0.3$  or  $0.1$ ) and adjusted sediment composition (i.e.,  $\sigma = 13.17$  or  
243  $4.25$  with  $d_{50} = 3.22$  mm) of the released debris flow, following the FBS cases.  
244 Details are summarized in Tables S4 and S5 in Supporting Information.

245

246

247 **FIGURE 2** Flume geometry used in (a) laboratory-scale numerical case studies  
248 (adapted from Iverson et al., 2011); (b) field-scale numerical case studies. The  
249 topography has an upstream ramp of uniform inclination angle  $\theta$ , length  $L_0$  and  
250 height  $H_0$ , followed by a horizontal runout pad at the downstream end.

251

## 252 **2.2 Modelling methods**

253 A depth-averaged two-phase flow model (Li et al., 2018a) is used to resolve the  
254 spatial and temporal evolution of debris flow, from initiation to final stoppage. The  
255 model is based on a previous fixed-bed model (Li, et al., 2018b), extended to erodible  
256 bed flows. On the basis of the numerical solutions, debris flow mobility and energy  
257 components can be readily determined. The present model is constructed according  
258 to continuum mechanics principles, in which inter-phase interaction is explicitly taken  
259 into account, unlike single-phase flow models (e.g., Takahashi et al., 1992; Iverson,  
260 1997; McDougall & Hungr, 2005; Medina et al., 2008; Armanini, 2009; Rosatti &  
261 Begnudelli, 2013; Iverson & George, 2014; Lucas et al., 2014; Frank et al., 2015;  
262 Cuomo et al., 2016; Xia et al., 2018; Federico & Cesali, 2019; Gregoretto et al., 2019).

263 Unlike existing two-phase flow models (Pitman & Le, 2005; Pelanti et al., 2008; Pailha  
264 & Pouliquen, 2009; Pudasaini, 2012; Kowalski & McElwaine, 2013; Bouchut et al.,  
265 2015), the present model incorporates multiple grain sizes (noting the typically broad  
266 distribution of grain size, which directly affects debris flow mobility (Johnson et al.,  
267 2012; de Haas et al., 2015; Kaitna et al., 2016)), mass exchange with the bed (that  
268 may affect mobility (Iverson, 1997; Hungr & Evans, 2004; Mangeney et al., 2007;  
269 Iverson et al., 2011; Lube et al., 2012)), and stresses due to strong liquid and solid  
270 fluctuations. The present model along with the governing equations are briefly  
271 described in Text S1 in Supporting Information.

272 A set of relationships is introduced to close the model, as is common with all such  
273 models in earth science. Although all the closure relations used in the two-phase flow  
274 model of Li et al. (2018a) were previously established for shallow water  
275 hydro-sediment-morphodynamics, some of them are also tentatively applied in debris  
276 flow modelling, and are inevitably empirical to some extent. We use the Coulomb  
277 friction law and Manning's equation to determine the bed shear stresses for solid and  
278 liquid phases respectively (Iverson, 1997; Pudasaini, 2012; Iverson & George, 2014).  
279 In practice, the Coulomb friction law is usually applied to friction-dominated debris  
280 flows. When debris flows are composed of coarse grains, they are mainly affected by  
281 a collisional, or a coupled frictional and collisional, regime (Lanzoni et al., 2017), for  
282 which a constitutive equation accounting for both the frictional and collisional stresses  
283 is warranted. Inter-phase interaction is modelled by means of the Gidaspow drag  
284 correlation (Gidaspow, 1994), which combines the Ergun equation for dense

285 water-sediment mixtures and a power law for dilute suspensions. Inter-grain size  
286 interaction is based on linear velocity-dependent drag, grain-grain surface interaction,  
287 and remixing force components (Gray & Chugunov, 2006). To date, there have been  
288 hardly any studies on inter-grain size interaction in debris flows. Thus, a closure  
289 relationship derived for a simple binary mixture (Gray & Chugunov, 2006) is  
290 tentatively used for debris flows (which are nevertheless composed of more broadly  
291 distributed grain sizes). Debris flows are characterized by strong fluctuations in liquid  
292 and solid motions (Iverson et al., 1997). However, generally valid closure models  
293 remain unavailable. By analogy to turbulent motion, the stress arising from liquid  
294 fluctuation is approximated by a conventional turbulent kinetic energy – dissipation  
295 rate ( $k - \varepsilon$ ) model (Rodi, 1993) originally developed for the flow of pure fluid without  
296 sediment. The stress due to solid fluctuation is determined by a first-order model  
297 based on the kinetic theory of granular flows under dilute flow conditions (Jenkins &  
298 Richman, 1985). Wu's formula (Wu, 2007) is used to estimate the sediment transport  
299 rate of each size fraction. An active layer formulation (Hirano, 1971) represents  
300 stratigraphic evolution of the bed. A plethora of closure relations has been proposed  
301 to estimate mass exchange with the bed induced by geophysical mass flows (see e.g.  
302 Pitman et al., 2003; McDougall & Hungr, 2005; Medina et al., 2008; Iverson, 2012;  
303 Pirulli & Pastor, 2012). Unfortunately, these relations suffer from shortcomings  
304 because understanding of the underlying physical processes remains far from clear  
305 (as discussed by e.g. Hungr & Evans, 2004; Iverson, 2012). Critically, most relations  
306 do not consider the effect of particle size, which is questionable from a physical

307 perspective because fine grains are easier to erode than large blocks (Pirulli & Pastor,  
308 2012). Given the fact that no generally valid mass exchange relations are available  
309 for erodible-bed debris flows, Li et al. (2018a) tentatively employed the closure model  
310 widely used in fluvial hydraulics to estimate mass exchange between the debris flow  
311 and the bed. This closure model has previously been found to perform significantly  
312 better than an alternative analytical relation (Medina et al., 2008).

313 The governing equations are numerically solved using an adapted version of a  
314 well-balanced numerical algorithm (Cao, P. Hu, K. Hu, Pender, & Liu, 2015a). The  
315 computational domain consists of a uniformly sloping ramp and adjacent  
316 (channelized) horizontal runout pad of unlimited length (Figures 1 and 2). For USGS  
317 debris flow experiments and laboratory-scale numerical cases, the spatial step  $\Delta x =$   
318 0.1 m, whereas for field-scale numerical cases,  $\Delta x = 0.4$  m. Numerical simulation is  
319 performed until the debris flow stops, at which time the run-out distance is evaluated.  
320 Initial values of flow thickness, volumetric sediment concentration, and bed elevation  
321 are case specific (see Tables S3-S5 in Supporting Information). The initial velocity,  
322 fluctuation kinetic energy, and dissipation rate are set to zero. Both the upstream and  
323 downstream boundary conditions are prescribed constant because the channel is  
324 sufficiently long to ensure that forward and backward waves of the debris flow do not  
325 reach either end boundary during the simulation.

326 Li et al. (2018a) provide a detailed description of the depth-averaged two-phase flow  
327 model equations along with model closure and the numerical algorithm. The model  
328 incorporates the leading-order physical factors in the mass and momentum

329 conservation equations, such as gravitation, resistance, inter-phase and inter-grain  
330 size interactions. Importantly, for the first time, this model performs well when tested  
331 against the full sets of USGS experimental debris flows over fixed-beds (Li et al.,  
332 2018b) and erodible-beds (Li et al., 2018a), and is able to resolve fundamental  
333 mechanisms in debris flows (e.g., significant effects of multiple grain sizes, bed  
334 erosion and initial water content) that have been found by observed field data  
335 (Iverson, 1997). It is nevertheless appreciated that more delicate and refined  
336 mechanisms may exist in debris flows, which, if incorporated, could modify the  
337 modelling results (e.g., collisional solid stress (Lanzoni et al., 2017) and  
338 non-Newtonian liquid viscous stress (Pudasaini, 2012)). However, these are most  
339 likely to be second- and higher-order factors; it is our intention to incorporate these in  
340 a future version of the model.

341 Note that compared with the friction coefficient values previously used (Li et al.,  
342 2018a), the values adopted in the present study have been slightly adjusted within  
343 the conventional range to reduce the residual bulk energy of debris flow to a minimum,  
344 while ensuring the computed kinetic variables (e.g., velocity, thickness, bed  
345 deformation, sediment concentration) match measured data (Iverson et al., 2011).  
346 Briefly, the Manning roughness has been tuned by 5.7%, increasing from 0.028 to  
347  $0.0296 \text{ s.m}^{-1/3}$ , and the solid friction coefficient has been tuned by 7.7%, reducing  
348 from 0.839 to 0.774. In relation to Cases EXP-F and EXP-E, Figures S1 and S2 show  
349 time series of front locations and flow surface elevations above the bed predicted by  
350 the present two-phase flow equation (TPE) model using previous (Li et al., 2018a)  
351 and adjusted friction coefficients, along with measured data (Iverson et al., 2011). For



352 Case EXP-E, Figure S3 compares the measured bed elevation time histories with  
353 predictions by the TPE model, utilizing previous values of friction coefficient (Li et al.,  
354 2018a) and adjusted friction coefficients. As can be seen from Figures S1-S3, the  
355 computed results by the TPE model with adjusted friction coefficients agree rather  
356 well with measured data and predictions by TPE model with previous friction  
357 coefficients (Li et al., 2018a).

358

## 359 **2.3 Energy calculation**

360 We calculate the energy components from initiation to stoppage based on physical  
361 variables (e.g. bed elevation, flow depth, flow velocity, volumetric concentration,  
362 fluctuation kinetic energy, and dissipation rates of the liquid and solid phases)  
363 resolved using the depth-averaged two-phase flow model (Li et al., 2018a) described  
364 above. Kinetic energy ( $E_K$ ), fluctuation kinetic energy ( $E_{TK}$ ), gravitational potential  
365 energy ( $E_G$ ), and potential energy due to sediment exchange with the bed ( $E_{Gb}$ ) are  
366 evaluated by trapezoidal integration of local variables over space at a specific time.  
367 Energy dissipation due to bed resistance ( $E_R$ ) and fluctuation motions ( $E_D$ ) and the  
368 work done by inter-phase ( $E_{fs}$ ) and inter-grain size interaction forces ( $E_{ss}$ ) are  
369 calculated by integrating variables in both space and time, again using the trapezoidal  
370 rule. Details of the energy calculation methods are described as follows.

371

### 372 **2.3.1 Gravitational potential energy**

373 The gravitational potential energy of the solid phase in a debris flow system,  $E_{Gs}$ , at  
374 any time  $t$  is

375 
$$E_{Gs}(t) = \int [\sum_{k=1}^N \rho_s h_i C_{ki} g H_i B_i] \Delta x \quad (1)$$

376 where  $\Delta x$  is the length of the control volume (Figure 3); subscript  $i$  denotes the  
 377 control volume index; subscript  $k$  denotes the  $k$ -th sediment size within  $N$  size  
 378 classes; subscript  $s$  represents the solid phase;  $g$  is gravitational acceleration;  $h_i$   
 379 is debris flow depth of the  $i$ -th control volume;  $C_{ki}$  is depth-averaged size-specific  
 380 volumetric sediment concentration of the  $i$ -th control volume;  $\rho_s$  is density of the  
 381 solid phase;  $B_i$  is width of the  $i$ -th control volume;  $H_i$  is vertical distance between  
 382 the mass center of debris flow of the  $i$ -th control volume and the datum level (Figure  
 383 3) set at the horizontal elevation of the run-out pad.  $H_i$  is calculated from

384 
$$H_i = (h_i/2 + z_{bi}(t)) \cos \theta + (x_d - x_i) \sin \theta \quad (2)$$

385 where  $x_d$  is distance from the mass release point along the channel to the point  
 386 where the flow reaches the horizontal reference datum;  $\theta$  is the bed slope angle.

387 The gravitational potential energy of the liquid phase in the debris flow system,  $E_{Gf}$ ,  
 388 at any time  $t$  is

389 
$$E_{Gf}(t) = \int [\rho_f h_i C_{fi} g H_i B_i] \Delta x \quad (3)$$

390 where subscript  $f$  represents the liquid phase; and  $C_{fi}$  is the depth-averaged  
 391 volume fraction of the liquid phase of the  $i$ -th control volume.

392

393

394 **FIGURE 3** Sketch of control volume used for energy calculation.  $H_i$  is vertical  
 395 distance between the mass center of debris flow of the  $i$ -th control volume and the  
 396 datum level, and is accordingly defined by Eq. (2).

397

### 398 **2.3.2 Kinetic energy**

399 The kinetic energy of the solid phase of the debris flow system,  $E_{Ks}$ , is calculated as

$$400 \quad E_{Ks}(t) = \int \left[ \sum_{k=1}^N \left( \frac{1}{2} \rho_s h_i C_{ki} U_{ski}^2 B_i \right) \right] \Delta x \quad (4)$$

401 where  $U_{ski}$  is the size-specific depth-averaged velocity of the solid phase in the  $x$ -  
402 direction of the  $i$ -th control volume. Likewise, the kinetic energy of the liquid phase  
403 of the debris flow system,  $E_{Kf}$ , at any time is defined as

$$404 \quad E_{Kf}(t) = \int \left[ \frac{1}{2} \rho_f h_i C_{fi} U_{fi}^2 B_i \right] \Delta x \quad (5)$$

405 where  $U_{fi}$  is the depth-averaged velocity of liquid phase in the  $x$ -direction of the  
406  $i$ -th control volume.

407

### 408 **2.3.3 Fluctuation kinetic energy**

409 Kinetic energy due to fluctuations of solid motions in the debris flow system is  
410 calculated by

$$411 \quad E_{TKs}(t) = \int \left[ \sum_{k=1}^N (\rho_s h_i C_{ki} TK_{ski} B_i) \right] \Delta x \quad (6)$$

412 where  $TK_{ski}$  is the size-specific depth-averaged fluctuation kinetic energy of the solid  
413 phase of the  $i$ -th control volume. The fluctuation kinetic energy of the liquid phase in  
414 the debris flow system is determined by

415 
$$E_{TK_f}(t) = \int [\rho_f h_i C_{fi} TK_{fi} B_i] \Delta x \quad (7)$$

416 where  $TK_{fi}$  is the depth-averaged fluctuation kinetic energy of the liquid phase of the  
 417  $i$  – th control volume.

418

### 419 **2.3.4 Potential energy due to sediment exchange with the bed**

420 In general, two distinct mechanisms are involved in sediment exchange with the bed:  
 421 sediment entrainment due to inter-phase and inter-grain size interactions; and  
 422 sediment deposition resulting primarily from gravitational action. Physically, eroded  
 423 bed sediments can increase the potential energy of debris flow which may be  
 424 converted into kinetic energy downslope, and *vice versa*. Similar to the calculation of  
 425 the potential energy of debris flow, the potential energy due to sediment exchange  
 426 with the bed is

427 
$$E_{Gb}(t) = \int [\rho_0 h_{bi} g H_{bi} B_i] \Delta x \quad (8)$$

428 where subscript  $b$  refers to bed material;  $\rho_0 = \rho_f \theta_f + \rho_s (1 - p)$  is the bed density,  
 429  $p$  is bed sediment porosity,  $\theta_f$  is water content of the bed (normally  $\theta_f \leq p$ ),  
 430  $h_{bi} = z_{bi}(t=0) - z_{bi}(t)$  is bed deformation depth; and  $z_{bi}$  is bed elevation of the  $i$  – th  
 431 control volume.  $H_{bi}$  is the vertical distance between the mass center of the  $i$  – th  
 432 control volume for bed deformation and the datum level, and is accordingly defined as  
 433 follows (Figure S4)

434 
$$H_{bi} = (h_{bi}/2 + z_{bi}(t)) \cos \theta + (x_d - x_i) \sin \theta \quad (9)$$

435

436 **2.3.5 Energy dissipation due to bed resistance and fluctuation motions**

437 During a time interval  $\Delta t$ , the liquid phase and size-specific solid phase travel  
 438 distances  $U_{fi}\Delta t$  and  $U_{ski}\Delta t$  over the bed, and so the energy loss due to bed  
 439 resistance in a unit volume during a time interval is defined as

440 
$$E_{Ri,\Delta t} = \tau_{fbi} U_{fi} B_i \Delta x \Delta t + \sum_{k=1}^N \tau_{skbi} U_{ski} B_i \Delta x \Delta t \quad (10)$$

441 where  $\tau_{fbi}$  and  $\tau_{skbi}$  are bed shear stresses for the liquid and size-specific solid  
 442 phases of the  $i$ -th control volume. Therefore, the time-dependent energy loss of  
 443 the debris flow system, induced by bed resistance, is

444 
$$E_R(t) = \iint [\tau_{fbi} U_{fi} B_i + \sum_{k=1}^N \tau_{skbi} U_{ski} B_i] \Delta x \Delta t \quad (11)$$

445 Likewise, the energy dissipation due to fluctuations is

446 
$$E_D(t) = \iint [\rho_f h_i C_{fi} \varepsilon_{fi} B_i + \sum_{k=1}^N \rho_s h_i C_{ski} \varepsilon_{ski} B_i] \Delta x \Delta t \quad (12)$$

447 where  $\varepsilon_{fi}$  and  $\varepsilon_{ski}$  are depth-averaged dissipation rates for the liquid and solid  
 448 phases, respectively.

449

450 **2.3.6 Work done by inter-phase and inter-grain size interactions**

451 The work done by the interaction force can be computed in a similar way to the  
 452 energy loss induced by bed resistance. For size-specific solid grains, the interaction  
 453 forces of the  $i$ -th control volume include a size-specific depth-averaged interphase  
 454 interaction force component  $F_{fski}$  for the solid phase and a size-specific

455 depth-averaged inter-grain size interaction force component  $F_{s-s_k i}$ , exerted on the  
 456  $k$  – th solid phase by the other solid-phase constituents, and which satisfies  
 457  $\sum (F_{s-s_k i}) = 0$ . Thus for the solid phase of the debris flow system, the work done by  
 458 the inter-phase interaction force is

$$459 \quad E_{fs} = \iint \left[ \sum_{k=1}^N F_{fs_{ki}} U_{skt} B_i \right] \Delta x \Delta t \quad (13)$$

460 and the work done by the inter-grain size interaction force is

$$461 \quad E_{ss} = \iint \left[ \sum_{k=1}^N F_{s-s_{ki}} U_{skt} B_i \right] \Delta x \Delta t \quad (14)$$

462 For the liquid phase, the interaction force of the  $i$  – th control volume consists of the  
 463 sum of interphase interaction forces,  $\sum F_{s_k f i}$ . Accordingly, the work done by the  
 464 interphase interaction force is

$$465 \quad E_{sf} = \iint \left[ \sum_{k=1}^N F_{s_k f i} U_{f i} B_i \right] \Delta x \Delta t \quad (15)$$

### 466 **2.3.7 Energy change**

467 The energy change in the debris flow relative to initial conditions is defined as

$$468 \quad \Delta E = E_G + E_K + E_{TK} + E_R + E_D - E_{T0} - E_{Gb} \quad (16)$$

469 where  $E_{T0}$  denotes the initial energy of debris flow. Energy changes of the solid  
 470 phase,  $\Delta E_s$ , the liquid phase,  $\Delta E_f$ , and the size-specific grains  $\Delta E_{sk}$  are similarly  
 471 defined.

472

## 473 3 RESULTS

### 474 3.1 Debris flow mobility reconstructed without utilizing reduced friction 475 coefficients

476 We reconstruct the relation between debris flow mobility and initial volume. In the  
477 experimental (Table S2) and numerical cases (Tables S3-S5), the volumes are based  
478 on distinct channel widths, in accordance with observed natural debris flows (Iverson,  
479 1997). To eliminate potential discrepancy due to different channel widths, we define  
480 the non-dimensional initial volume  $\hat{V}_0$  as  $\hat{V}_0 = \bar{V}_0 / V_{ref}$ , where  $\bar{V}_0$  is the initial volume  
481 per unit width and  $V_{ref}$  is that of a reference case (i.e., Case EXP-F), i.e.,  $V_{ref} = 3 \text{ m}^2$ .  
482 Similarly, the non-dimensional run-out distance  $\hat{L}$  is defined as  $\hat{L} = L / L_{ref}$ , where  
483  $L_{ref}$  is the run-out distance in Case EXP-F. Figure 4 shows the dependence of debris  
484 flow mobility, characterized by efficiency  $e$  (Figure 4a) and run-out distance  $\hat{L}$   
485 (Figure 4b), on non-dimensional initial volume over a  $31^\circ$  sloping ramp. Figure S5  
486 presents the corresponding results for a  $40^\circ$  sloping ramp. In agreement with  
487 observations (Iverson 1997; Lucas et al., 2014), the mobility computed using the  
488 two-phase flow model (Li et al., 2018a) described above increases progressively as  
489 initial volume increases. Obviously, a debris flow over a steep slope has higher  
490 mobility than its mild-slope counterpart when all other conditions remain the same (c.f.  
491 results Tables S3-S5). Bed erosion, water content, and grain-size heterogeneity also  
492 enhance debris flow mobility, echoing previous findings from field and experimental  
493 data (Iverson, 1997; Legros, 2002; Rickenmann, 2005). When the initial volume is  
494 sufficiently small, the efficiency remains constant because the debris flow would  
495 terminate on the sloping ramp before reaching the runout pad, and so  $e = \cot \theta = 1.664$ .  
496 Moreover, predictions from three typical empirical relationships (Corominas, 1996;

497 Rickmann, 1999; Lucas et al., 2014) are included for comparison, which are unable to  
498 resolve the effects of bed erosion, water content, and grain-size heterogeneity. It can  
499 be seen that the computed efficiency for fixed-bed debris flows agrees with the most  
500 recently derived empirical relationship, based on velocity-dependent friction  
501 weakening (Lucas et al., 2014) (Table S6). However, whilst Figure 4 and Figure S5  
502 show a positive correlation between mobility (in terms of efficiency  $e$  and run-out  
503 distance  $\hat{L}$ ) and initial volume, the data fail to collapse on a single curve. Arguably,  
504 this is because the correlation between mobility and initial volume is purely  
505 geometrical, and does not contain any information relating to debris flow dynamics  
506 (Staron & Lajeunesse, 2007). In light of these results, it is suggested that initial  
507 volume alone is inadequate to characterize debris flow mobility.

508  
509  
510 **FIGURE 4.** Dependence of debris flow mobility on initial volume over a 31° sloping  
511 ramp. (a) Debris flow efficiency  $e$  against non-dimensional initial volume  $\hat{V}_0$ . Solid,  
512 dotted and dashed lines respectively present empirical results for laboratory-scale,  
513 intermediate and large field-scale cases. (b) Non-dimensional debris flow run-out  
514 distance  $\hat{L}$  against non-dimensional initial volume  $\hat{V}_0$ .

515

### 516 **3.2 Debris flow energetics: Grain-energy release**

517 We probe into the energetics of the USGS large-scale experimental debris flows  
518 (Iverson et al., 2011) by evaluating the evolution of energy components and energy  
519 changes per unit width for both fixed-bed Case EXP-F (Figure 5) and erodible bed  
520 Case EXP-E (Figure 6).

521 The energy is conserved from initiation to final stoppage, characterizing the energy  
522 balance, as illustrated by  $\Delta E \approx \Delta E_s + \Delta E_f \approx 0$  (Figures 5b and 6b). For the fixed-bed



523 case, Figure 5a, the gravitational potential energy  $E_G$  of both the liquid and solid  
524 phases decreases monotonically, being progressively transformed into kinetic energy  
525 ( $E_K$ ) and fluctuation energy ( $E_{TK}$ ), and dissipated by bed resistance ( $E_R$ ) and  
526 fluctuation motions ( $E_D$ ). For the erodible-bed case, Figure 6a shows that  $E_G$  initially  
527 decreases, then increases due to bed erosion, peaks and subsequently decreases as  
528 the debris flow peters out. Meanwhile,  $E_G$  and, where applicable, the potential  
529 energy of the eroded material  $E_{Gb}$ , are gradually converted into kinetic energy ( $E_K$ )  
530 and fluctuation energy ( $E_{TK}$ ), and dissipated by bed resistance ( $E_R$ ) and fluctuation  
531 motions ( $E_D$ ), similar to the fixed-bed case. Note that  $E_{TK}$  is negligible, even though  
532 its effect on debris flow kinetics is discernible (Li et al., 2018a).

533 Most notably, we find that the grains as a whole release energy to the liquid phase at  
534 debris flow stoppage. For the liquid phase, the energy change  $\Delta E_f > 0$  at stoppage  
535 (i.e.,  $t = 40$  s), indicating that energy dissipated by bed resistance and fluctuation  
536 motions ( $E_{Rf} + E_{Df}$ ) exceeds the initial bulk energy ( $E_{T0f}$ ) (Figure 5b, for the fixed-bed  
537 case) and, where applicable, the potential energy of the eroded bed material ( $E_{Gb}$ )  
538 (Figure 6b, for the erodible-bed case). For the solid phase, the reverse occurs as  
539  $\Delta E_s < 0$ . Moreover, the magnitudes of  $\Delta E_s$  and  $\Delta E_f$  are comparable with the peak  
540 kinetic energy. Note that mass gain from bed erosion enhances energy transfer  
541 because the grain-energy release of the erodible-bed case at stoppage (Figure 6b) is  
542 considerably greater than its fixed-bed counterpart (Figure 5b).

543 Further, the energy change of the liquid phase  $\Delta E_f$  is approximately equal to the  
544 work done by solid-liquid interaction,  $E_{sf}$ , indicating that  $\Delta E_f$  arises from  
545 interaction with the solid phase. Concurrently, the energy change of the solid phase

546  $\Delta E_s$  is equal to the work done by liquid-solid interaction and interactions between  
547 different-sized grains, i.e.,  $E_{fs} + E_{ss}$ . Physically, the sum of interactive forces between  
548 the liquid and solid grains and between different-sized grains must vanish according  
549 to Newton's third law. However, the liquid and different-sized grains typically have  
550 distinct velocities and so their interactive forces generate energy transfer. Noting that  
551 previous studies reveal that water content and grain-size heterogeneity can enhance  
552 debris flow mobility (Iverson, 1997; Legros, 2002; Rickenmann, 2005), the present  
553 work suggests that it is the interactions between liquid and solid grains and between  
554 different-sized grains that enable the effects of water content and grain-size  
555 heterogeneity on debris flow mobility to be substantial.

556 Inter-phase energy transfer is a highly complex process. For the fixed-bed case  
557 (Figure 5b), the transfer process involves three stages. First,  $\Delta E_s$  increases and  
558  $\Delta E_f$  decreases. Initially, the liquid moves freely and propagates faster downslope  
559 than the solid grains; hence the solid-liquid interactive force  $F_{sf} < 0$ , and accordingly  
560  $E_{sf} < 0$ , leading to a decrease in  $\Delta E_f$ . The growth in  $\Delta E_s$  primarily arises from  $E_{fs}$ ,  
561 which increases because the liquid-solid interactive force  $F_{fs} > 0$  while  $E_{ss}$   
562 decreases with time. During the second stage, the energy changes of both phases  
563 exhibit reverse behavior, i.e.,  $\Delta E_s$  decreases and  $\Delta E_f$  increases. Due to energy  
564 gain during the first stage, the solid grains gradually move faster than the liquid phase.  
565 Consequently  $F_{sf} > 0$  and the liquid phase absorbs energy from the solid phase;  
566 meanwhile  $\Delta E_s$  reduces mainly due to inter-phase and inter-grain size interactions.  
567 Finally, when the debris flow gradually comes to rest, causing deposition on the  
568 runout pad, both  $\Delta E_f$  and  $\Delta E_s$  become steady. Comparatively, in the erodible-bed

569 case (Figure 6b), at the early stage,  $t < 0.6$  s, when the debris flow reaches the  
570 erodible bed but erosion has not yet commenced, the debris flow exhibits similar  
571 inter-phase energy transfer features to those observed during the first two stages of  
572 the fixed-bed debris flow (Figure 5b), i.e.,  $\Delta E_s$  increases initially and then decreases,  
573 whereas  $\Delta E_f$  undergoes the opposite behaviour. Subsequently, a new cycle of  
574 three-stage inter-phase energy transfer, similar to that in fixed-bed debris flow, is  
575 triggered by rapid bed erosion and proceeds until the debris flow comes to a halt.

576

577

578 **FIGURE 5** Evolution of energy components and energy changes of USGS  
579 experimental fixed-bed debris flows Case EXP-F (Iverson et al., 2011). (a) Evolution  
580 of energy components, including kinetic energy ( $E_K$ ), fluctuation kinetic energy ( $E_{TK}$ ),  
581 gravitational potential energy ( $E_G$ ), and energy dissipation due to bed resistance ( $E_R$ )  
582 and fluctuation motions ( $E_D$ ) with the subscripts  $f$  and  $s$  denoting the liquid and  
583 solid phases, respectively. (b) Evolution of energy changes of the solid-liquid mixture  
584 ( $\Delta E$ ), solid phase ( $\Delta E_s$ ), and liquid phase ( $\Delta E_f$ ), and the work done by inter-phase  
585 ( $E_{fs}$  and  $E_{sf}$ ) and inter-grain size interaction forces ( $E_{ss}$ ).

586

587

588 **FIGURE 6** Evolution of energy components and energy changes of USGS  
589 experimental erodible-bed debris flows Case EXP-E (Iverson et al., 2011). (a)  
590 Evolution of energy components, including kinetic energy ( $E_K$ ), fluctuation kinetic  
591 energy ( $E_{TK}$ ), gravitational potential energy ( $E_G$ ), potential energy due to sediment  
592 exchange with the bed ( $E_{Gb}$ ), and energy dissipation due to bed resistance ( $E_R$ ) and  
593 fluctuation motions ( $E_D$ ) with the subscripts  $f$  and  $s$  denoting the liquid and solid  
594 phases, respectively. (b) Evolution of energy changes of the solid-liquid mixture ( $\Delta E$ ),  
595 solid phase ( $\Delta E_s$ ), and liquid phase ( $\Delta E_f$ ), and the work done by inter-phase ( $E_{fs}$

596 and  $E_{sf}$ ) and inter-grain size interaction forces ( $E_{ss}$ ).

597

598 The role of grains in debris flow energetics is size-dependent (Figures 7 and 8).

599 During the initial stage, the liquid phase releases energy to grains of all sizes as  $E_{fsk}$

600 increases; and fine grains release energy to coarse grains as  $E_{ssk}$  decreases for fine

601 grains (Figures 7a-b and Figures 8a-b) and increases for coarse grains (Figures 7c-d

602 and Figures 8c-d). Besides,  $E_{fsk} + E_{ssk}$  of fine grains decreases, whereas that of

603 coarse grains increases, indicating that fine grains release energy while coarse grains

604 absorb energy. Physically, this process lubricates the grains, especially coarse grains,

605 and facilitates the initiation and acceleration of debris flow, as evidenced by an

606 increase in kinetic energy (Figure 5b and Figure 6b). Subsequently, reverse energy

607 transfer is exhibited as the grains release energy to the liquid, and coarse grains

608 transfer energy to fine grains, sustaining the debris flow until it stops, during which

609 time the bulk kinetic energy decreases (Figure 5b and Figure 6b). Specifically,  $E_{fsk}$  of

610 all grains and  $E_{ssk}$  of coarse grains decrease (Figures 7c-d and Figures 8c-d), while

611  $E_{ssk}$  of fine grains increases (Figures 7a-b and Figures 8a-b). Also,  $E_{fsk} + E_{ssk}$  of fine

612 grains increases, while that of coarse grains decreases. Note that the mass gain from

613 bed erosion enhances such processes because the magnitudes of  $E_{fsk}$ ,  $E_{ssk}$  and

614  $E_{fsk} + E_{ssk}$  in the erodible-bed case (Figure 8) are generally larger than their

615 counterparts in the fixed-bed case (Figure 7). Until final stoppage, coarse grains

616 release energy over both fixed and erodible beds because  $E_{fsk} + E_{ssk} < 0$  (Figures 7c-d

617 and Figures 8c-d), whereas fine grains in the erodible-bed case release energy

618 because  $E_{fsk} + E_{ssk} < 0$ , as shown in Figures 8a-b, contrary to fine grains absorbing

619 energy in the fixed-bed case (see Figures 7a-b).

620

621

622 **FIGURE 7** Evolution of energy changes in size-specific grains for fixed-bed Case  
623 EXP-F. (a-b) fine grains; (c-d) coarse grains.  $E_{fsk}$  and  $E_{sfk}$  represent work done by  
624 the inter-phase interaction force, and  $E_{ssk}$  represents work done by the inter-grain  
625 size interaction force.

626

627

628 **FIGURE 8** Evolution of energy changes in size-specific grains for erodible-bed Case  
629 EXP-E. (a-b) fine grains; (c-d) coarse grains.  $E_{fsk}$  and  $E_{sfk}$  represent work done by  
630 the inter-phase interaction force, and  $E_{ssk}$  represents work done by the inter-grain  
631 size interaction force.

632

633

### 634 **3.3 Grain-energy release as a function of initial volume**

635 We now evaluate the grain-energy release for all the numerical cases (Table S3-S5).

636 The non-dimensional grain-energy release is defined as  $\Delta\hat{E}_s = \text{abs}(\Delta E_s) / \text{abs}(E_{ref})$ ,

637 where  $E_{ref}$  is the grain-energy release in Case EXP-F. The dependence of

638 non-dimensional grain-energy release  $\Delta\hat{E}_s$  on initial volume is illustrated for the two

639 ramps in Figure 9 and Figure S6. Similar to debris flow mobility (Figure 4 and Figure

640 S5), grain-energy release increases with initial debris flow volume and ramp length,

641 and is enhanced by mass gain from bed erosion, water content, and grain-size

642 heterogeneity. Furthermore, the steeper ramp usually leads to elevated grain-energy

643 release (comparing Figure 9 to Figure S6).

644

645

646 **FIGURE 9** Dependence of non-dimensional grain-energy release  $\Delta\hat{E}_s$  on  
647 non-dimensional initial debris flow volume  $\hat{V}_0$  over a 31° sloping ramp.

648

### 649 **3.4 Debris flow mobility correlated with grain-energy release**

650 We now delve into the relationship between debris flow mobility and grain-energy  
651 release at final stoppage. Interestingly, the mobility of debris flow correlates closely  
652 with grain-energy release in terms of both efficiency  $e$  (Figure 10a) and run-out  
653 distance  $\hat{L}$  (Figure 10b).

654 As shown in Figure 10a, when the initial volume is very small, the efficiency is  
655 determined solely by slope angle, i.e.,  $e = \cot \theta$ . For intermediate initial volumes, the  
656 efficiency is jointly determined by initial volume and ramp length; therefore, it follows  
657 different relations with non-dimensional grain-energy release, depending on ramp  
658 length, but independent of mass gain from bed erosion, water content, grain-size  
659 heterogeneity, and ramp slope angle. If the initial volume is sufficiently large, its effect  
660 on efficiency reigns over the ramp, rendering a collapse of the data from both  
661 laboratory- and field-scale cases onto a single curve. Therefore, the non-dimensional  
662 grain-energy release, which incorporates the effects of initial volume and topography,  
663 is more suitable than initial volume alone for characterizing the mobility of debris flow.  
664 This proposition is further reinforced by the universal relation between run-out  
665 distance and grain energy release ( $\hat{L} \sim \Delta\hat{E}_s$ ) shown in Figure 10b, regardless of ramp  
666 length, slope angle, initial volume, water content, bed erosion, and grain-size  
667 heterogeneity.

668 Given the above observations, we propose that grain-energy release governs debris  
669 flow mobility, therefore facilitating a bridge between debris flow mobility and internal

670 energy transfer. It is well recognized that experimental observation of grain-energy  
671 release of debris flow is much more challenging than that of the initial volume. This is  
672 perhaps why debris flow energetics have rarely, if ever, been related to debris flow  
673 mobility. Therefore, this topic invites future investigation as driven from the present  
674 findings. Indeed, it is quite common that computational science leads to new theories  
675 and inspires new experiments, or suggests important variables to be investigated in  
676 laboratory tests.

677

678

679 **FIGURE 10** Debris flow mobility versus grain-energy release. (a) Dependence of  
680 efficiency  $e$  on non-dimensional grain-energy release  $\Delta\hat{E}_s$ ; (b) Dependence of  
681 non-dimensional run-out distance  $\hat{L}$  on non-dimensional grain-energy release  $\Delta\hat{E}_s$ .

682

## 683 4 DISCUSSION

### 684 4.1 Inter-phase energy transfer

685 The results in Section 3.2 lead us to propose an energy transfer pattern between  
686 liquid, fine grains, and coarse grains in debris flow (Figure 11). During the initial stage  
687 of a mass-release debris flow, the liquid phase transfers energy to the grains, and fine  
688 grains release energy to coarse grains. Later, the grains release energy to the liquid,  
689 and coarse grains release energy to fine grains, thus sustaining the debris flow until  
690 final stoppage. Up to final stoppage, the coarse grains release energy ( $E_{fsk} + E_{ssk} < 0$ ),  
691 whilst the fine grains either absorb ( $E_{fsk} + E_{ssk} > 0$ ) or release ( $E_{fsk} + E_{ssk} < 0$ ) energy,  
692 depending on bed erosion (Figures 7 and 8); and concurrently, among those grains  
693 releasing energy, the larger the grain size, the higher the grain energy release, and  
694 this grain-size dependence can be modified by initial volume, water content,

695 grain-size heterogeneity, and bed erosion (Figure S7). The energy transfer pattern  
696 appears to underpin previous experimental findings (Iverson, 1997; Johnson et al.,  
697 2012; de Haas et al., 2015; Kaitna et al., 2016) that interactions between fine and  
698 coarse grains can increase debris flow mobility.

699

700

701 **FIGURE 11** Energy transfer between liquid, fine grains, and coarse grains in debris  
702 flow.

703

#### 704 **4.2 Implications**

705 Our finding that grain-energy release governs high mobility of debris flow provides  
706 insight into the fundamental mechanisms of debris flows due to solid-liquid mass  
707 release. In particular, initial volume, as a univariate variable, is inadequate for  
708 characterizing debris flow mobility. The grain-energy release appears to be more  
709 suitable. Furthermore, a friction-reduction mechanism (e.g., Legros, 2002; Iverson et  
710 al., 2011; Lube et al., 2012; Pudasaini & Miller, 2013; Lucas et al., 2014) is not a  
711 prerequisite for the high mobility of debris flows. By contrast, inter-phase and  
712 inter-grain size interactions play primary roles and so should be explicitly incorporated  
713 in debris flow models. This implies that existing quasi single-phase models (e.g.,  
714 Takahashi et al., 1992; Iverson, 1997; McDougall & Hungr, 2005; Medina et al., 2008;  
715 Armanini, 2009; Rosatti & Begnudelli, 2013; Iverson & George, 2014; Lucas et al.,  
716 2014; Frank et al., 2015; Cuomo et al., 2016; Xia et al., 2018; Federico & Cesali, 2019;  
717 Gregoretto et al., 2019), two-phase models that presume a single grain size (e.g.,



718 Pitman & Le, 2005; Pelanti et al., 2008; Pailha & Pouliquen, 2009; Pudasaini, 2012;  
719 Kowalski & McElwaine, 2013; Bouchut et al., 2015), and energy balance-based  
720 models (Wang et al., 2010; Bouchut et al., 2015) may need to be enhanced for more  
721 accurate resolution of debris flows. Likewise, additional large-scale debris flow  
722 experiments using flumes with varied bed topography and observations of natural  
723 debris flows over irregular and steep slopes are needed in order to support further  
724 model development. Indeed, the present modelling results inevitably bear some  
725 degree of uncertainty because empirical closures for inter-grain size interaction, liquid  
726 and solid fluctuations, and mass exchange with the bed have tentatively been used.  
727 Therefore, this topic invites more systematic fundamental investigation. As multiple  
728 physics are involved in the present model, scaling analysis is required to evaluate  
729 their relative importance in resolving the mechanisms underlying the high mobility of  
730 debris flows due to solid-liquid mass release.

731 The first of its kind, the present work has implications in future assessments of debris  
732 flow hazards and in informing mitigation and adaptation strategies. This is significant  
733 and particularly timely, noting the acceleration in glacier melt and increasing trend in  
734 extreme precipitation amount, intensity, and frequency (Donat et al., 2013), which are  
735 likely to trigger more debris flows. The study also has broad implications for  
736 unravelling a spectrum of earth surface processes including heavily sediment-laden  
737 floods due to storms and glacier lake outbursts (Larone & Reid, 1993; Xiao, Young,  
738 & Prévost, 2010; Grinsted, Hvidberg, Campos, Dahl-Jensen, 2017; Cook, Andermann,  
739 Gimbert, Adhikari, & Hovius, 2018; Hook, 2019), and subaqueous debris flows and

740 turbidity currents in rivers, reservoirs, estuaries, and the ocean (Weirich, 1988; Wright  
741 & Friedrichs, 2006; Talling et al., 2007; Armanini, 2013; Cao, Li, Pender, & Liu, 2015b;  
742 Paull et al., 2018; Stevenson et al., 2018; Li, Cao, & Liu, 2019).

743

## 744 **5 CONCLUSIONS**

745 A recently developed depth-averaged two-phase flow model has been used to  
746 investigate debris flow mobility, without evoking reduced friction coefficients. Debris  
747 flow mobility computed by the model increases with initial volume and is enhanced by  
748 mass gain from bed erosion, water content, and grain-size heterogeneity, echoing  
749 previous experimental and field studies. It is found that whilst the energy balance  
750 holds and fine and coarse grains play distinct roles in debris flow energetics, the  
751 grains as a whole release energy to the liquid due to inter-phase and inter-grain size  
752 interactions, and the grain-energy release correlates closely with debris flow mobility.  
753 This leads us to propose that the mobility of debris flow due to solid-liquid mass  
754 release is governed by grain-energy release, thereby facilitating a bridge between  
755 debris flow mobility and internal energy transfer.

756 Grain-energy release appears to be more suitable than initial volume to characterize  
757 debris flow mobility. Also, grain-energy release characterizes the interactions  
758 between liquid and solid grains and between different-sized grains, which play  
759 primary roles in debris flow dynamics. In light of the present finding from  
760 physically-based numerical modelling, the quest for a friction-reduction mechanism  
761 may not be viable, which concurs with Iverson (2016) who comments that there is  
762 insufficient experimental evidence to support the friction-reduction hypotheses.  
763 Meanwhile, it is implied that single-phase flow models, two-phase flow models that

764 presume a single grain size, and energy balance-based models may need to be  
765 enhanced for resolving debris flows and hence assessment of such hazards.

766 Although the closure models are far from perfect, the findings obtained from the  
767 present model are qualitatively encouraging and physically meaningful. Indeed, all  
768 models for earth surface flows inevitably contain uncertainty arising from empirical  
769 closure, which invites systematic fundamental investigation in the future. Further  
770 experiments are needed to enhance the understanding of debris flows and to further  
771 validate the present findings. Moreover, as multiple physics are involved in the  
772 present model, scaling analysis is required to evaluate their relative importance in  
773 debris flow dynamics. Extension to two dimensions would be useful for practical  
774 applications to natural debris flows.

775

## 776 **ACKNOWLEDGEMENTS**

777 This study was supported by Natural Science Foundation of China under Grants NO.  
778 11672212 and 11432015.

779

## 780 **DATA AVAILABILITY STATEMENT**

781 The data that support the findings of this study are available from the corresponding  
782 author upon reasonable request.

783

784 **NOTATION**

$B_i$	width of the $i$ -th control volume (m)
$C_k$	depth-averaged size-specific volumetric sediment concentration (-)
$C_f$	depth-averaged volume fraction of the liquid phase (-)
$d_{50}$	particle size at which 50% of the sediments are finer (m)
$e$	debris flow efficiency (-)
$E_D$	energy dissipation due to fluctuation motions (J)
$E_{fs}$	work done by inter-phase interaction force for the solid phase (J)
$E_G$	gravitational potential energy of debris flow (J)
$E_{Gb}$	potential energy due to sediment exchange with the bed (J)
$E_{Gs}, E_{Gf}$	gravitational potential energy of the solid and liquid phases in debris flow (J)
$E_k$	kinetic energy of debris flow (J)
$E_{ks}, E_{kf}$	kinetic energy of the solid and liquid phases in debris flow (J)
$E_R$	energy dissipation due to bed resistance (J)
$E_{sf}$	work done by inter-phase interaction force for the liquid phase (J)
$E_{ss}$	work done by inter-grain size interaction force (J)
$E_{T0}$	initial energy of debris flow (J)
$E_{TK}$	fluctuation kinetic energy of debris flow (J)
$E_{TKs}, E_{TKf}$	fluctuation kinetic energy of the solid and liquid phases debris flow (J)
$F_{fsk}$	size-specific depth-averaged interphase interaction force for the solid phase ( $\text{kg m}^{-1} \text{s}^{-2}$ )
$F_{s_kf}$	size-specific depth-averaged interphase interaction force for the liquid phase ( $\text{kg m}^{-1} \text{s}^{-2}$ )
$F_{s-s_k}$	size-specific depth-averaged inter-grain size interaction drag force ( $\text{kg m}^{-1} \text{s}^{-2}$ )

$f, s, m$	subscript denoting the liquid phase, solid phase, mixture (-)
$g$	gravitational acceleration ( $\text{ms}^{-2}$ )
$H_i$	vertical distance between the mass center of debris flow of the $i$ -th control volume and the datum level (m)
$H_{bi}$	vertical distance between the mass center of the $i$ -th control volume for bed deformation and the datum level (m)
$h$	debris flow depth (m)
$h_b$	bed deformation depth (m)
$i$	index denoting the control volume (-)
$k$	subscript denoting the $k$ -th sediment size
$L$	run-out distance of debris flow (m)
$L_{ref}$	run-out distance of debris flow of a reference case (m)
$\hat{L}$	non-dimensional run-out distance of debris flow
$p$	porosity of bed sediments (-)
$TK_{sk}$	size-specific depth-averaged fluctuation kinetic energy of the solid phase ( $\text{m}^2 \text{s}^{-3}$ )
$TK_f$	depth-averaged fluctuation kinetic energy of the liquid phase ( $\text{m}^2 \text{s}^{-3}$ )
$t$	time (s)
$U_f$	depth-averaged velocity of the liquid phase in the $x$ -direction ( $\text{m s}^{-1}$ )
$U_{sk}$	size-specific depth-averaged velocity of the solid phase in the $x$ -direction ( $\text{m s}^{-1}$ )
$\bar{V}_0$	initial volume per unit width ( $\text{m}^2$ )
$\hat{V}_0$	non-dimensional initial volume
$V_b$	volume of bed sediments ( $\text{m}^3$ )
$\bar{V}_{ref}$	initial volume per unit width of a reference case
$x$	streamwise coordinate (m)
$x_d$	distance from the mass release point along the channel to the point where the flow reaches the horizontal reference datum (m)

$z_b$	bed elevation (m)
$\Delta E_f$	energy change of the liquid phase in debris flow (J)
$\Delta E_s$	energy change of the solid phase in debris flow (J)
$\Delta \hat{E}_s$	non-dimensional grain-energy release (-)
$\Delta E_{sk}$	energy change of size-specific grains (J)
$\Delta t$	time step (s)
$\Delta x$	spatial step (m)
$\varepsilon_f$	depth-averaged dissipation rate of liquid fluctuation kinetic energy ( $\text{m}^2 \text{s}^{-3}$ )
$\varepsilon_{sk}$	Size-specific depth-averaged dissipation rate of solid fluctuation kinetic energy ( $\text{m}^2 \text{s}^{-3}$ )
$\theta$	angle of bed slope (-)
$\theta_f$	water content of bed sediments (-)
$\sigma$	standard deviation of sediment composition (-)
$\rho_f, \rho_s$	densities of the liquid and solid phases ( $\text{kg m}^{-3}$ )
$\tau_{s_k b}, \tau_{fb}$	bed shear stresses for the solid and liquid phases respectively ( $\text{kg m}^{-1} \text{s}^{-2}$ )

785

786

787

788 **REFERENCES**

- 789 Armanini, A. (2013). Granular flows driven by gravity. *Journal of Hydraulic Research*,  
790 51(2), 111-120. doi: 10.1080/00221686.2013.788080
- 791 Armanini, A., Fraccarollo, L., & Rosatti, G. (2009). Two-dimensional simulation of  
792 debris flows in erodible channels. *Computers & Geosciences*, 35(5), 993-1006.  
793 doi: 10.1016/j.cageo.2007.11.008
- 794 Bouchut, F., Fernandez-Nieto, E. D., Mangeney, A., & Narbona-Reina, G. (2015). A  
795 two-phase shallow debris flow model with energy balance. *ESAIM: Mathematical*  
796 *Modelling and Numerical Analysis*, 49(1), 101-140. doi: 10.1051/m2an/2014026
- 797 Cao, Z., Hu, P., Hu, K., Pender, G., & Liu, Q. (2015a). Modelling roll waves with  
798 shallow water equations and turbulent closure. *Journal of Hydraulic Research*,  
799 53(2), 161-177 (2015). doi: 10.1080/00221686.2014.950350.
- 800 Cao, Z., Li, J., Pender, G., & Liu, Q. (2015b). Whole-process modeling of reservoir  
801 turbidity currents by a double layer-averaged model. *Journal of Hydraulic*  
802 *Engineering*, 141(2), 04014069. doi: 10.1061/(ASCE)HY.1943-7900.0000951.
- 803 Chen, M., Liu, X., Wang, X., Zao, T., & Zhou, J. (2019). Contribution of Excessive  
804 Supply of Solid Material to a Runoff-Generated Debris Flow during Its Routing  
805 Along a Gully and Its Impact on the Downstream Village with Blockage Effects.  
806 *Water*, 11(1), 169. doi:10.3390/w11010169
- 807 Cook, K. L., Andermann, C., Gimbert, F., Adhikari, B. R., & Hovius, N. (2018). Glacial  
808 lake outburst floods as drivers of fluvial erosion in the Himalaya. *Science*,  
809 362(6410), 53-57. doi: 10.1126/science.aat4981.



810 Corominas, J. (1996). The angle of reach as a mobility index for small and large  
811 landslides. *Canadian Geotechnical Journal*, 33(2), 260-271. doi:  
812 10.1139/t96-005.

813 Cuomo, S., Pastor, M., Capobianco, V., & Cascini, L. (2016). Modelling the space-  
814 time bed entrainment for flow-like landslide. *Engineering Geology*, 212, 10-20.  
815 doi: 10.1016/j.enggeo.2016.07.011.

816 de Haas, T., Braat, L., Leuven, J. R., Lokhorst, I. R., & Kleinhans, M. G. (2015).  
817 Effects of debris flow composition on runout, depositional mechanisms, and  
818 deposit morphology in laboratory experiments. *Journal of Geophysical Research:*  
819 *Earth Surface*, 120(9), 1949-1972. doi: 10.1002/2015JF003525.

820 Donat, M. G., Alexander, L. V., Yang, H., Durre, I., Vose, R., Dunn, R. J. H., ... &  
821 Hewitson, B. (2013). Updated analyses of temperature and precipitation extreme  
822 indices since the beginning of the twentieth century: The HadEX2 dataset.  
823 *Journal of Geophysical Research: Atmospheres*, 118(5), 2098-2118. doi:  
824 10.1002/jgrd.50150

825 Federico, F., & Cesali, C. (2019). Effects of granular collisions on the rapid  
826 coarse-grained materials flow. *Géotechnique Letters*, 9(4), 1-6. doi:  
827 10.1680/jgele.18.00223.

828 Frank, F., McArdell, B.W., Huggel, C., & Vieli, A. (2015). The importance of  
829 entrainment and bulking on debris flow runout modeling: examples from the  
830 Swiss Alps. *Natural Hazards and Earth System Sciences*, 15(11), 2569-2583.  
831 doi:10.5194/nhess-15-2569-2015.

832 Gidaspow, D. (1994). *Multiphase Flow and Fluidization: Continuum and Kinetic*  
833 *Theory Descriptions*. Cambridge, MA: Academic Press.

- 834 Goren, L., & Aharonov, E. (2007). Long runout landslides: the role of frictional heating  
835 and hydraulic diffusivity. *Geophysical Research Letters*, 34(7), 248-265. doi:  
836 10.1029/2006GL02889
- 837 Gray, J. M. N. T., & Chugunov, V. A. (2006). Particle-size segregation and diffusive  
838 remixing in shallow granular avalanches. *Journal of Fluid Mechanics*, 569,  
839 365-398. doi: 10.1017/S0022112006002977.
- 840 Gregoretti, C., Degetto, M., Bernard, M., & Boreggio, M. (2018). The debris flow  
841 occurred at Ru Secco Creek, Venetian Dolomites, on 4 August 2015: analysis of  
842 the phenomenon, its characteristics and reproduction by models. *Frontier in*  
843 *Earth Sciences*, 6, 80. doi: 10.3389/feart.2018.00080.
- 844 Gregoretti, C., Stancanelli, L., Bernard, M., Degetto, M., Boreggio, M., & Lanzoni, S.  
845 (2019). Relevance of erosion processes when modelling in-channel gravel debris  
846 flows for efficient hazard assessment. *Journal of Hydrology*, 568, 575-591;  
847 doi10.1016/j.jhydrol.2018.10.001
- 848 Grinsted, A., Hvidberg, C. S., Campos, N., & Dahl-Jensen, D. (2017). Periodic  
849 outburst floods from an ice-dammed lake in East Greenland. *Scientific reports*,  
850 7(1), 9966. doi: 10.1038/s41598-017-07960-9
- 851 Hayashi, J. N., & Self, S. (1992). A comparison of pyroclastic flow and debris  
852 avalanche mobility. *Journal of Geophysical Research: Solid Earth*, 97(B6),  
853 9063-9071. doi: 10.1029/92JB00173
- 854 Hirano, M. (1971). River bed degradation with armouring. *Transactions of Japanese*  
855 *Society of Civil Engineering*, 195(11), 55-65 (in Japanese).
- 856 Hook, J. M. (2019). Extreme sediment fluxes in a dryland flash flood. *Scientific*  
857 *Reports*, 9, 1686. doi: 10.1038/s41598-019-38537-3
- 858 Hungr, O., & Evans, S. G. (2004). Entrainment of debris in rock avalanches: an

859 analysis of a long run-out mechanism. *Geological Society of America Bulletin*,  
860 116(9-10), 1240-1252. doi: 10.1130/B25362.1.

861 Hürlimann, M., Abanco, C., Moya, J., & Vilajosana, I. (2014). Results and experiences  
862 gathered at the Rebaixader debris-flow monitoring site, Central Pyrenees, Spain.  
863 *Landslides*, 11(6), 161–175. <https://doi.org/10.1007/s10346-013-0452-y>.

864 Iverson, R. M. (1997). The physics of debris flows. *Reviews of geophysics*, 35(3),  
865 245-296. doi: 10.1029/97RG00426.

866 Iverson, R. M. (2012). Elementary theory of bed-sediment entrainment by debris  
867 flows and avalanches. *Journal of Geophysical Research: Earth Surface*, 117,  
868 F03006, doi:10.1029/2011JF002189.

869 Iverson, R. M. (2016). Comment on “The reduction of friction in long-runout landslides  
870 as an emergent phenomenon” by Brandon C. Johnson et al. *Journal of*  
871 *Geophysical Research: Earth Surface*, 121(11), 2238-2242. doi:  
872 10.1002/2016JF003979.

873 Iverson, R. M., & George, D. L. (2014). A depth-averaged debris-flow model that  
874 includes the effects of evolving dilatancy. I. Physical basis. *Proceedings of the*  
875 *Royal Society A: Mathematical, Physical and Engineering Sciences*, 470(2170),  
876 20130819. doi: 10.1098/rspa.2013.0819.

877 Iverson, R. M., George, D. L., Allstadt, K., Reid, M. E., Collins, B. D., Vallance, J.  
878 W., ... & Baum, R. L. (2015). Landslide mobility and hazards: implications of the  
879 2014 Oso disaster. *Earth and Planetary Science Letters*, 412, 197-208. doi:  
880 10.1016/j.epsl.2014.12.020.

881 Iverson, R. M., Logan, M., LaHusen, R. G., & Berti, M. (2010). The perfect debris flow?

882 Aggregated results from 28 large-scale experiments. *Journal of Geophysical*  
883 *Research: Earth Surface*, 115(F3). doi: 10.1029/2009JF001514.

884 Iverson, R. M., Reid, M. E., Logan, M., LaHusen, R. G., Godt, J. W., & Griswold, J. P.  
885 (2011). Positive feedback and momentum growth during debris-flow entrainment  
886 of wet bed sediment. *Nature Geoscience*, 4(2), 116-121. doi: 10.1038/ngeo1040

887 Jenkins, J. T., & Richman, M. W. (1985). Grad's 13 moment system for a dense gas of  
888 inelastic spheres. *Archive for Rational Mechanics and Analysis*, 87, 355-377.

889 Johnson, B. C., Campbell, C. S., & Melosh, H. J. (2016). The reduction of friction in  
890 long runout landslides as an emergent phenomenon. *Journal of Geophysical*  
891 *Research: Earth Surface*, 121(5), 881-889. doi: 10.1002/2015JF003751.

892 Johnson, C. G., Kokelaar, B. P., Iverson, R. M., Logan, M., LaHusen, R. G., & Gray, J.  
893 M. N. T. (2012). Grain-size segregation and levee formation in geophysical mass  
894 flows. *Journal of Geophysical Research: Earth Surface*, 117(F01032). doi:  
895 10.1029/2011JF002185.

896 Kaitna, R., Palucis, M. C., Yohannes, B., Hill, K. M., & Dietrich, W. E. (2016). Effects  
897 of coarse grain size distribution and fine particle content on pore fluid pressure  
898 and shear behavior in experimental debris flows. *Journal of Geophysical*  
899 *Research: Earth Surface*, 121(2), 415-441. doi: 10.1002/2015JF003725.

900 Kowalski, J., & McElwaine, J. N. (2013). Shallow two-component gravity-driven flows  
901 with vertical variation. *Journal of Fluid Mechanics*, 714, 434-462. doi:  
902 10.1017/jfm.2012.489.

903 Kean, J. W., McCoy, S. W., Tucker, G. E., Staley, D. M., & Coe, J. A. (2013).  
904 Runoff-generated debris flows: Observations and modeling of surge initiation,  
905 magnitude, and frequency. *Journal of Geophysical Research: Earth Surface*, 118,  
906 2190–2207. doi:10.1002/jgrf.20148, 2013

907 Laronne, J. B., & Reid, I. (1993). Very high rates of bedload sediment transport by  
908 ephemeral desert rivers. *Nature*, 366, 148-150. doi: 10.1038/366148a0.

909 Lanzoni, S., Gregoretto, C., & Stancanelli, L. (2017). Coarse-grained debris flow  
910 dynamics on erodible beds. *Journal of Geophysical Research: Earth Surface*,  
911 122, 592-614, doi: 10.1002/2016JF004046.

912 Legros, F. (2002). The mobility of long-runout landslides. *Engineering Geology*, 63(3),  
913 301-331. doi: 10.1016/S0013-7952(01)00090-4.

914 Li, J., Cao, Z., & Liu, Q. (2019). Waves and sediment transport due to granular  
915 landslides impacting reservoirs. *Water Resources Research*, 55(1), 495-518. doi:  
916 10.1029/2018WR023191

917 Li, J., Cao, Z., Hu, K., Pender, G., & Liu, Q. (2018a). A depth-averaged two-phase  
918 model for debris flows over erodible bed. *Earth Surface Processes and  
919 Landforms*, 43(4), 817-839. doi: 10.1002/esp.4283.

920 Li, J., Cao, Z., Hu, K., Pender, G., & Liu, Q. (2018b). A depth-averaged two-phase  
921 model for debris flows over fixed beds. *International Journal of Sediment  
922 Research*, 33(4), 462-477. doi: 10.1016/j.ijsrc.2017.06.003.

923 Linares-Guerrero, E., Goujon, C., & Zenit, R. (2007). Increased mobility of bidisperse  
924 granular avalanches. *Journal of Fluid Mechanics*, 593, 475-504. doi:  
925 10.1017/S0022112007008932.

926 Lube, G., Cronin, S. J., Manville, V., Procter, J. N., Cole, S. E., & Freundt, A. (2012).  
927 Energy growth in laharcic mass flows. *Geology*, 40(5), 475-478. doi:  
928 10.1130/G32818.1.

929 Lucas, A., Mangeney, A., & Ampuero, J. P. (2014). Frictional velocity-weakening in  
930 landslides on Earth and on other planetary bodies. *Nature Communications*, 5(3),

931 3417. doi: 10.1038/ncomms4417.

932 Ma, C., Deng, J., & Wang, R. (2018). Analysis of the triggering conditions and erosion  
933 of a runoff triggered debris flow in Miyun County, Beijing, China. *Landslide*,  
934 *15*(12), 2475-2485. doi: 10.1007/s10346-018-1080-3.

935 Mangeney, A., Tsimring, L. S., Volfson, D., Aranson, I. S., & Bouchut, F. (2007).  
936 Avalanche mobility induced by the presence of an erodible bed and associated  
937 entrainment. *Geophysical Research Letters*, *34*, L22401. doi:  
938 10.1029/2007GL031348.

939 Medina, V., Hürlimann, M., & Bateman, A. (2008). Application of FLATModel, a 2D  
940 finite volume code, to debris flows in the northeastern part of the Iberian  
941 Peninsula. *Landslides*, *5*(1), 127-142. doi: 10.1007/s10346-007-0102-3.

942 McDougall, S., & Hungr, O. (2005). Dynamic modelling of entrainment in rapid  
943 landslides. *Canadian Geotechnical Journal*, *42*(5): 1437–1448. doi:  
944 10.1139/t05-064

945 Pailha, M., & Pouliquen, O. (2009). A two-phase flow description of the initiation of  
946 underwater granular avalanches. *Journal of Fluid Mechanics*, *633*, 115–135. doi:  
947 10.1017/S0022112009007460.

948 Paull, C. K., Talling, P. J., Maier, K. L., Parsons, D., Xu, J., Caress, D. W., ... & Chaffey,  
949 M. (2018). Powerful turbidity currents driven by dense basal layers. *Nature*  
950 *Communications*, *9*(1), 4114. doi: 10.1038/s41467-018-06254-6.

951 Pelanti, M., Bouchut, F., & Mangeney, A. (2008). A Roe-Type scheme for twophase  
952 shallow granular flows over variable topography. *ESAIM: Mathematical Modelling*  
953 *and Numerical Analysis*, *42*, 851–885. doi: 10.1051/m2an:2008029

954 Perinotto, H., Schneider, J. L., Bachèlery, P., Le Bourdonnec, F. X., Famin, V., &

955 Michon, L. (2015). The extreme mobility of debris avalanches: A new model of  
956 transport mechanism. *Journal of Geophysical Research: Solid Earth*, 120(12),  
957 8110-8119. doi: 10.1002/2015JB011994.

958 Pirulli, M., & Pastor M. (2012). Numerical study on the entrainment of bed material  
959 into rapid landslides. *Géotechnique*, 62(11), 959-972. doi:  
960 10.1680/geot.10.P.074.

961 Pitman, E. B., Nichita, C. C., Patra, A. K., Bauer, A. C., Bursik, M., & Weber, A. (2003).  
962 A model of granular flows over an erodible surface. *Discrete and Continuous*  
963 *Dynamical Systems Series B*, 3(4), 589-600. doi: 10.3934/dcdsb.2003.3.589.

964 Pitman, E. B., & Le, L. (2005). A two-fluid model for avalanche and debris flows.  
965 *Proceedings of the Royal Society of London A: Mathematical, Physical and*  
966 *Engineering Sciences*, 363, 1573–1602. doi: 10.1098/rsta.2005.1596

967 Pudasaini, S. P. (2012). A general two-phase debris flow model. *Journal of*  
968 *Geophysical Research: Earth Surface*, 117, F03010. doi:  
969 10.1029/2011JF002186.

970 Pudasaini, S. P., & Miller, S. A. (2013). The hypermobility of huge landslides and  
971 avalanches. *Engineering Geology*, 157, 124-132. doi:  
972 10.1016/j.enggeo.2013.01.012.

973 Rickenmann, D. (1999). Empirical relationships for debris flows. *Natural hazards*,  
974 19(1), 47-77. doi: 10.1023/A:100806422.

975 Rickenmann, D. (2005). Runout prediction methods. In M. Jakob, & O. Hungr (Eds.),  
976 *Debris-Flow Hazards and Related Phenomena* (pp. 305-324). Berlin, Heidelberg:  
977 Springer

978 Rodi, W. (1993). *Turbulence models and their application in hydraulics*. Boca Raton,  
979 Florida: CRC Press.

980 Rosatti, G., & Begnudelli, L. (2013). Two-dimensional simulation of debris flows over  
981 erodible bed: enhancing the TRENT2D model by using a well-balanced  
982 generalized Roe-type solver. *Computers and Fluids*, 71, 179–195. doi:  
983 10.1016/j.compfluid.2012.10.006.

984 Staron, L., & Lajeunesse, E. (2009). Understanding how volume affects the mobility of  
985 dry debris flows. *Geophysical Research Letters*, 36(12), L12402.  
986 doi:10.1029/2009GL038229.

987 Shreve, R. L. (1968). Leakage and fluidization in air-layer lubricated avalanches.  
988 *Geological Society of America Bulletin*, 79(5), 653-658. doi:  
989 10.1130/0016-7606(1968)79[653:LAFIAL]2.0.CO;2.

990 Singer, K. N., McKinnon, W. B., Schenk, P. M., & Moore, J. M. (2012). Massive ice  
991 avalanches on lapetus mobilized by friction reduction during flash heating.  
992 *Nature Geoscience*, 5(8), 574-578. doi: 10.1038/ngeo1526.

993 Stevenson, C. J., Feldens, P., Georgiopoulou, A., Schönke, M., Krastel, S., Piper, D.  
994 J., ... & Mosher, D. (2018). Reconstructing the sediment concentration of a giant  
995 submarine gravity flow. *Nature Communications*, 9(1), 2616. doi:  
996 10.1038/s41467-018-05042-6.

997 Talling, P. J., Wynn, R. B., Masson, D. G., Frenz, M., Cronin, B. T., Schiebel, R., ... &  
998 Georgiopoulou, A. (2007). Onset of submarine debris flow deposition far from  
999 original giant landslide. *Nature*, 450(7169), 541-544. doi: 10.1038/nature06313.

1000 Takahashi, T., Nakagawa, H., Harada, T., & Yamashiki, Y. (1992). Routing debris  
1001 flows with particle segregation. *Journal of Hydraulic Engineering*, 118(11),  
1002 1490–1507. doi: 10.1061/(ASCE)0733-9429(1992)118:11(1490)



- 1003 Utili, S., Zhao, T., & Houlsby, G. T. (2015). 3D DEM investigation of granular column  
1004 collapse: evaluation of debris motion and its destructive power. *Engineering*  
1005 *Geology*, 186, 3-16. doi: 10.1016/j.enggeo.2014.08.018
- 1006 Vallance, J. W., & Scott, K. M. (1997). The Osceola Mudflow from Mount Rainier:  
1007 Sedimentology and hazard implications of a huge clay-rich debris flow.  
1008 *Geological Society of America Bulletin*, 109(2), 143-163. doi:  
1009 10.1130/0016-7606(1997)109<0143:TOMFMR>2.3.CO;2.
- 1010 Wang, X., Morgenstern, N. R., & Chan, D. H. (2010). A model for geotechnical  
1011 analysis of flow slides and debris flows. *Canadian Geotechnical Journal*, 47(12),  
1012 1401-1414. doi: 10.1139/T10-039.
- 1013 Wang, Y. F., Dong, J. J., & Cheng, Q. G. (2017). Velocity-dependent frictional  
1014 weakening of large rock avalanche basal facies: Implications for rock avalanche  
1015 hypermobility? *Journal of Geophysical Research: Solid Earth*, 122(3), 1648-1676.  
1016 doi: 10.1002/2016JB013624
- 1017 Weirich, H. H. (1988). Field evidence for hydraulic jumps in subaqueous sediment  
1018 gravity flows. *Nature*, 332, 626-629. doi: 10.1038/332626a0
- 1019 Wright, L. D., & Friedrichs, C. T. (2006). Gravity-driven sediment transport on  
1020 continental shelves: a status report. *Continental Shelf Research*, 26(17-18),  
1021 2092-2107. doi: 10.1016/j.csr.2006.07.008.
- 1022 Wu, W. (2007). *Computational river dynamics*. London: Taylor & Francis.
- 1023 Xia, C.C., Li, J., Cao, Z., Liu, Q., & Hu, K. (2018). A quasi single-phase model for  
1024 debris flows and its comparison with a two-phase model. *Journal of Mountain*

1025            *Science*, 15(5), 1071-1089. doi: 10.1007/s11629-018-4886-5

1026    Xiao, H., Young, Y. L., & Prévost, J. H. (2010). Hydro-and morpho-dynamic modeling

1027            of breaking solitary waves over a fine sand beach. Part II: Numerical simulation.

1028            *Marine Geology*, 269(3-4), 119-131. doi: 10.1016/j.margeo.2009.12.008.

1029

1030

1031

1032 **List of figure captions**

1033 **FIGURE 1** Flume geometry for USGS debris flow experiments [from Iverson et al.  
1034 (2011)].

1035

1036 **FIGURE 2** Flume geometry used in (a) laboratory-scale numerical case studies  
1037 (adapted from Iverson et al., 2011); (b) field-scale numerical case studies. The  
1038 topography has an upstream ramp of uniform inclination angle  $\theta$ , length  $L_0$  and  
1039 height  $H_0$ , followed by a horizontal runout pad at the downstream end.

1040

1041 **FIGURE 3** Sketch of control volume used for energy calculation.  $H_i$  is vertical  
1042 distance between the mass center of debris flow of the  $i$ -th control volume and the  
1043 datum level, and is accordingly defined by Eq. (3).

1044

1045 **FIGURE 4.** Dependence of debris flow mobility on initial volume over a  $31^\circ$  sloping  
1046 ramp. (a) Debris flow efficiency  $e$  against non-dimensional initial volume  $\hat{V}_0$ . Solid,  
1047 dotted and dashed lines respectively present the empirical results for laboratory-scale,  
1048 intermediate and large field-scale cases. (b) Non-dimensional debris flow run-out  
1049 distance  $\hat{L}$  against non-dimensional initial volume  $\hat{V}_0$ .

1050

1051 **FIGURE 5** Evolution of energy components and energy changes of USGS  
1052 experimental fixed-bed debris flows Case EXP-F (Iverson et al., 2011). (a) Evolution  
1053 of energy components, including kinetic energy ( $E_K$ ), fluctuation kinetic energy ( $E_{TK}$ ),  
1054 gravitational potential energy ( $E_G$ ), and energy dissipation due to bed resistance ( $E_R$ )  
1055 and fluctuation motions ( $E_D$ ) with the subscripts  $f$  and  $s$  denoting the liquid and  
1056 solid phases, respectively. (b) Evolution of energy changes of the solid-liquid mixture  
1057 ( $\Delta E$ ), solid phase ( $\Delta E_s$ ), and liquid phase ( $\Delta E_f$ ), and the work done by inter-phase  
1058 ( $E_{fs}$  and  $E_{sf}$ ) and inter-grain size interaction forces ( $E_{ss}$ ).

1059

1060 **FIGURE 6** Evolution of energy components and energy changes of USGS  
1061 experimental erodible-bed debris flows Case EXP-E (Iverson et al., 2011). (a)  
1062 Evolution of energy components, including kinetic energy ( $E_K$ ), fluctuation kinetic

1063 energy ( $E_{TK}$ ), gravitational potential energy ( $E_G$ ), potential energy due to sediment  
 1064 exchange with the bed ( $E_{Gb}$ ), and energy dissipation due to bed resistance ( $E_R$ ) and  
 1065 fluctuation motions ( $E_D$ ) with the subscripts  $f$  and  $s$  denoting the liquid and solid  
 1066 phases, respectively. (b) Evolution of energy changes of the solid-liquid mixture ( $\Delta E$ ),  
 1067 solid phase ( $\Delta E_s$ ), and liquid phase ( $\Delta E_f$ ), and the work done by inter-phase ( $E_{fs}$   
 1068 and  $E_{sf}$ ) and inter-grain size interaction forces ( $E_{ss}$ ).

1069  
 1070 **FIGURE 7** Evolution of energy changes in size-specific grains for fixed-bed Case  
 1071 EXP-F. (a-b) fine grains; (c-d) coarse grains.  $E_{fsk}$  and  $E_{sfk}$  represent work done by  
 1072 the inter-phase interaction force, and  $E_{ssk}$  represents work done by the inter-grain  
 1073 size interaction force.

1074  
 1075 **FIGURE 8** Evolution of energy changes in size-specific grains for erodible-bed Case  
 1076 EXP-E. (a-b) fine grains; (c-d) coarse grains.  $E_{fsk}$  and  $E_{sfk}$  represent work done by  
 1077 the inter-phase interaction force, and  $E_{ssk}$  represents work done by the inter-grain  
 1078 size interaction force.

1079  
 1080 **FIGURE 9** Dependence of non-dimensional grain-energy release  $\Delta \hat{E}_s$  on  
 1081 non-dimensional initial debris flow volume  $\hat{V}_0$  over a  $31^\circ$  sloping ramp.

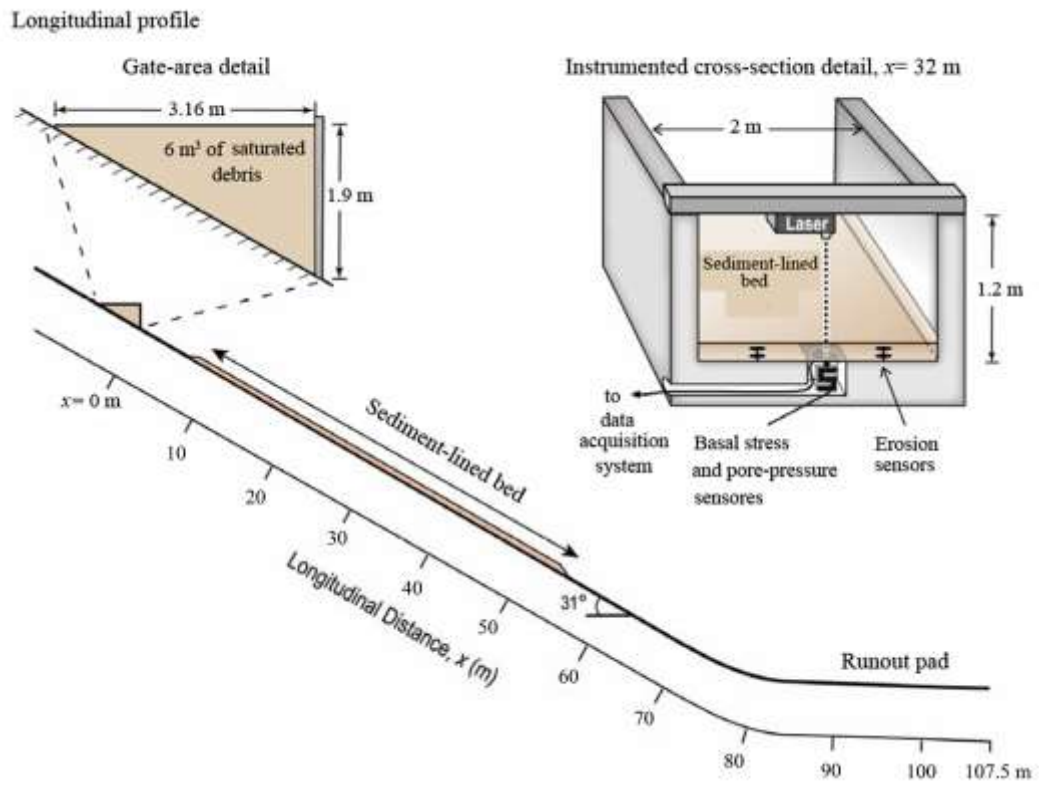
1082  
 1083 **FIGURE 10** Debris flow mobility versus grain-energy release. (a) Dependence of  
 1084 efficiency  $e$  on non-dimensional grain-energy release  $\Delta \hat{E}_s$ ; (b) Dependence of  
 1085 non-dimensional run-out distance  $\hat{L}$  on non-dimensional grain-energy release  $\Delta \hat{E}_s$ .

1086  
 1087 **FIGURE 11** Energy transfer between liquid, fine grains, and coarse grains in debris  
 1088 flow.

1089

1090 **FIGURES**

1091



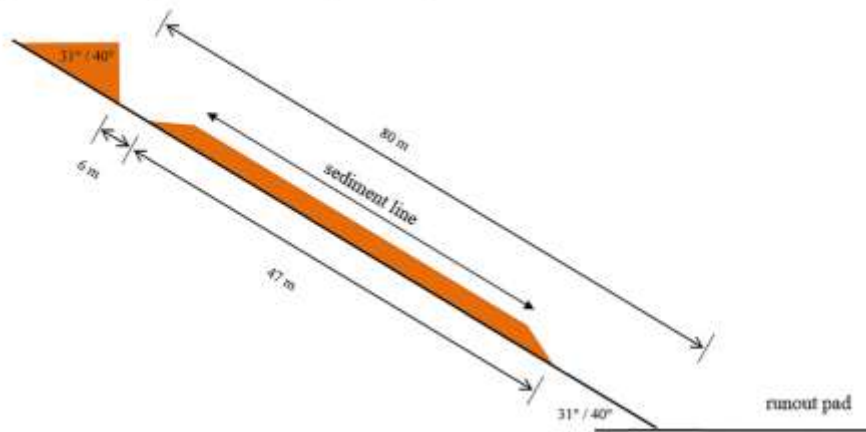
1092

1093 **FIGURE 1** Flume geometry for USGS debris flow experiments [from Iverson et al.

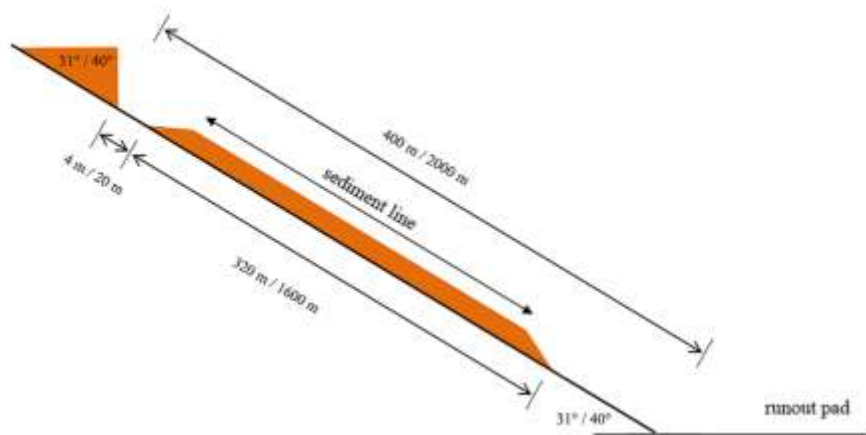
1094 (2011)].

1095

(a) Laboratory-scale flume geometry



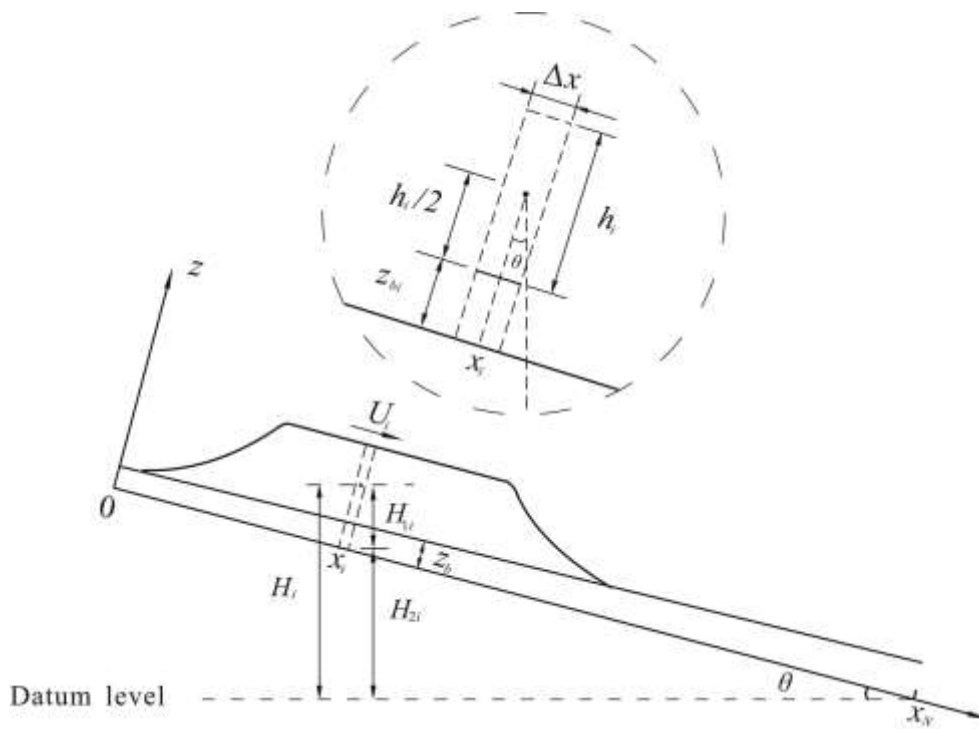
(b) Field-scale flume geometry



1096

1097 **FIGURE 2** Flume geometry used in (a) laboratory-scale numerical case studies  
1098 (adapted from Iverson et al., 2011); (b) field-scale numerical case studies. The  
1099 topography has an upstream ramp of uniform inclination angle  $\theta$ , length  $L_0$  and  
1100 height  $H_0$ , followed by a horizontal runout pad at the downstream end.

1101



1102

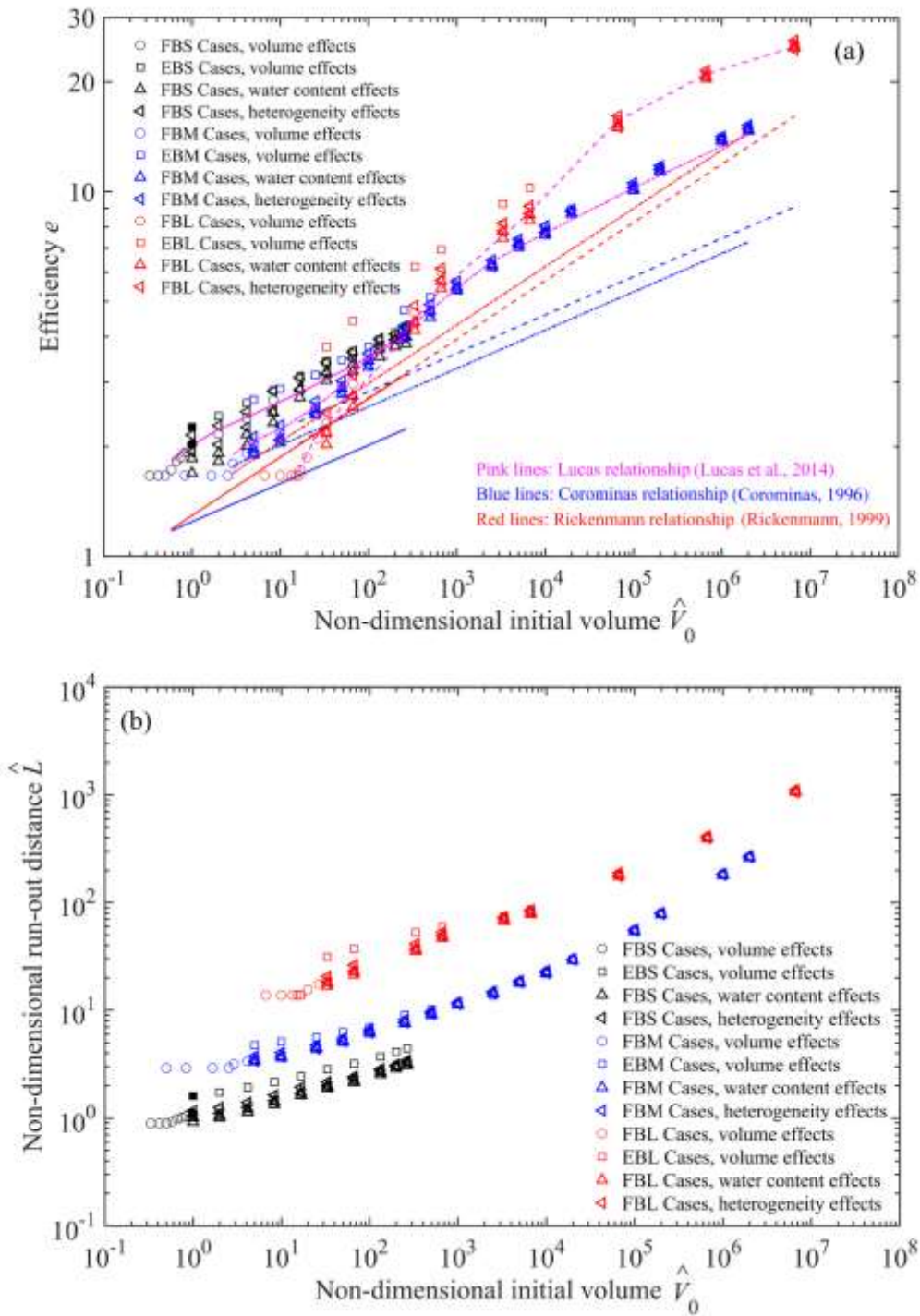
1103

**FIGURE 3** Sketch of control volume used for energy calculation.  $H_i$  is vertical distance between the mass center of debris flow of the  $i$ -th control volume and the datum level, and is accordingly defined by Eq. (2).

1104

1105

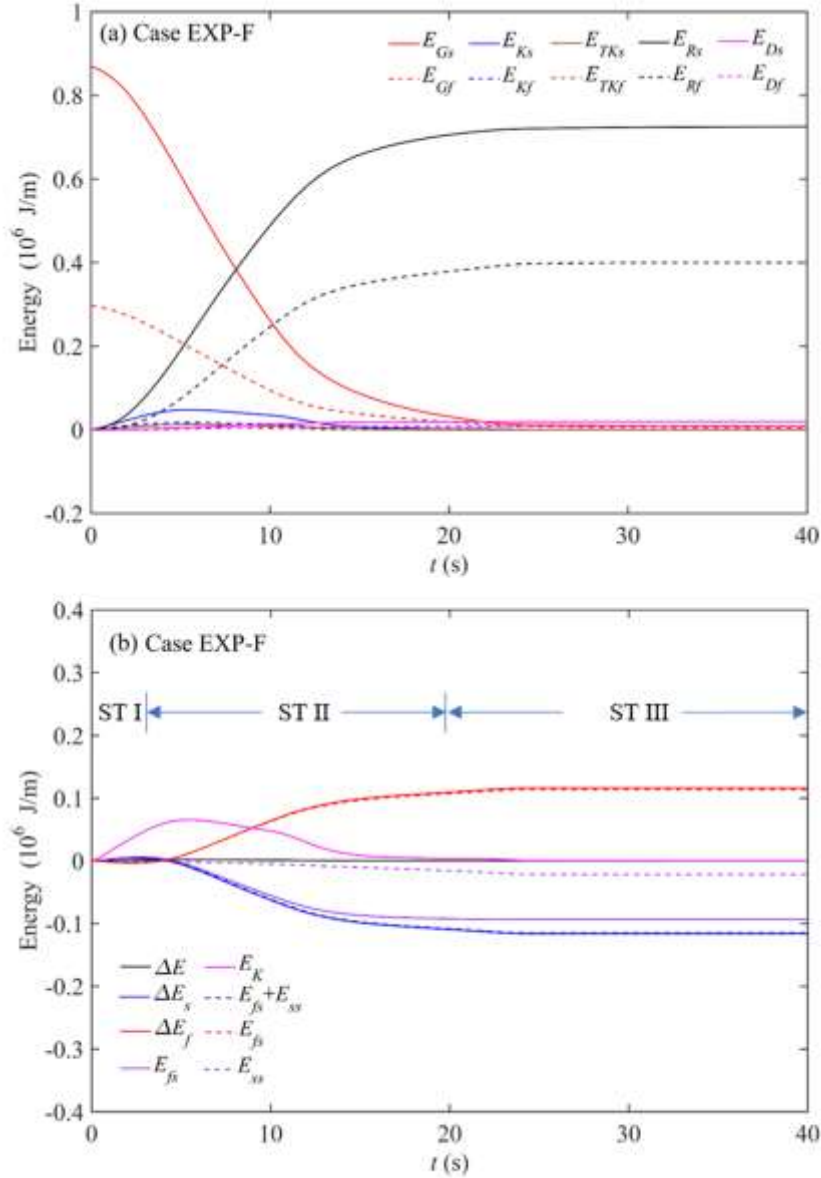
1106



1107  
 1108 **FIGURE 4.** Dependence of debris flow mobility on initial volume over a 31° sloping  
 1109 ramp. (a) Debris flow efficiency  $e$  against non-dimensional initial volume  $\hat{V}_0$ . Solid,  
 1110 dotted and dashed lines respectively denote empirical results for laboratory-scale,  
 1111 intermediate and large field-scale cases. (b) Non-dimensional debris flow run-out  
 1112 distance  $\hat{L}$  against non-dimensional initial volume  $\hat{V}_0$ .

1113





1114

1115 **FIGURE 5** Evolution of energy components and energy changes of USGS

1116 experimental fixed-bed debris flows Case EXP-F (Iverson et al., 2011). (a) Evolution

1117 of energy components, including kinetic energy ( $E_K$ ), fluctuation kinetic energy ( $E_{TK}$ ),

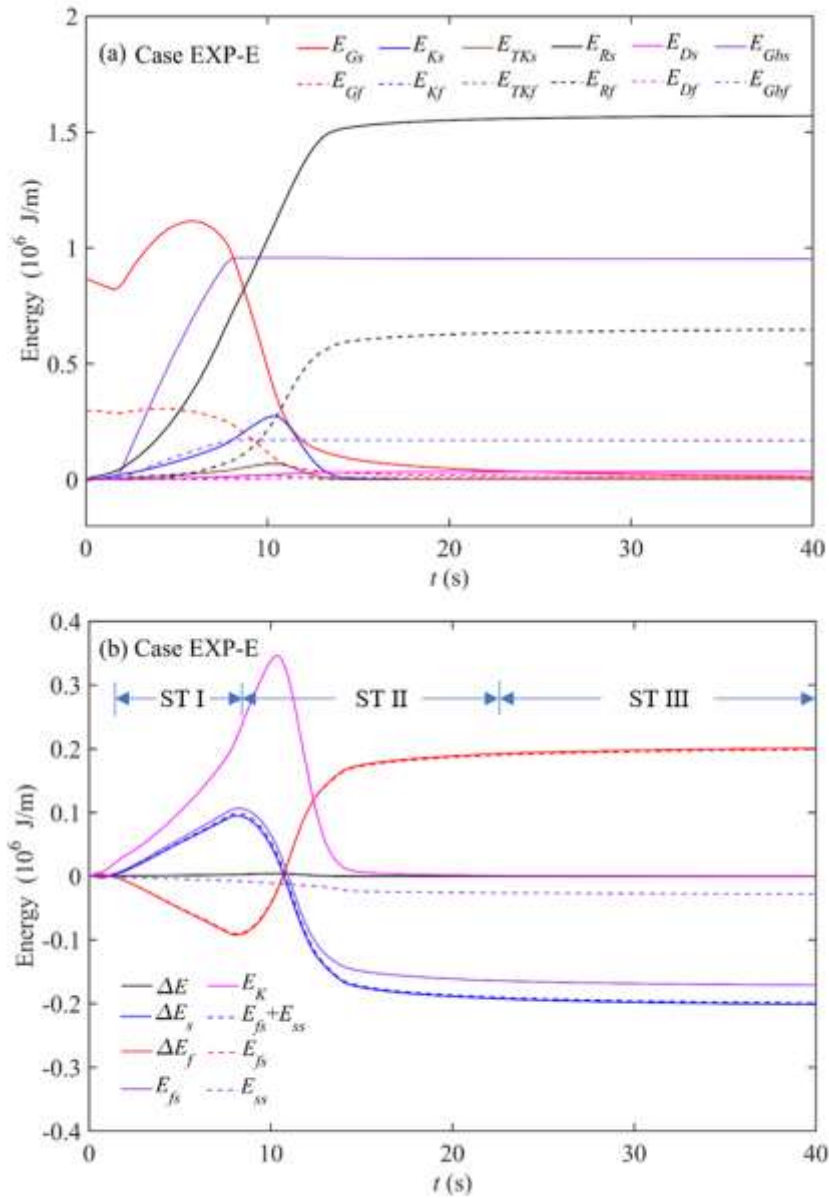
1118 gravitational potential energy ( $E_G$ ), and energy dissipation due to bed resistance ( $E_R$ )

1119 and fluctuation motions ( $E_D$ ) with the subscripts  $f$  and  $s$  denoting the liquid and

1120 solid phases, respectively. (b) Evolution of energy changes of the solid-liquid mixture

1121 ( $\Delta E$ ), solid phase ( $\Delta E_s$ ), and liquid phase ( $\Delta E_f$ ), and the work done by inter-phase

1122 ( $E_{fs}$  and  $E_{sf}$ ) and inter-grain size interaction forces ( $E_{ss}$ ).



1123

1124 **FIGURE 6** Evolution of energy components and energy changes of USGS

1125 experimental erodible-bed debris flows Case EXP-E (Iverson et al., 2011). (a)

1126 Evolution of energy components, including kinetic energy ( $E_K$ ), fluctuation kinetic

1127 energy ( $E_{TK}$ ), gravitational potential energy ( $E_G$ ), potential energy due to sediment

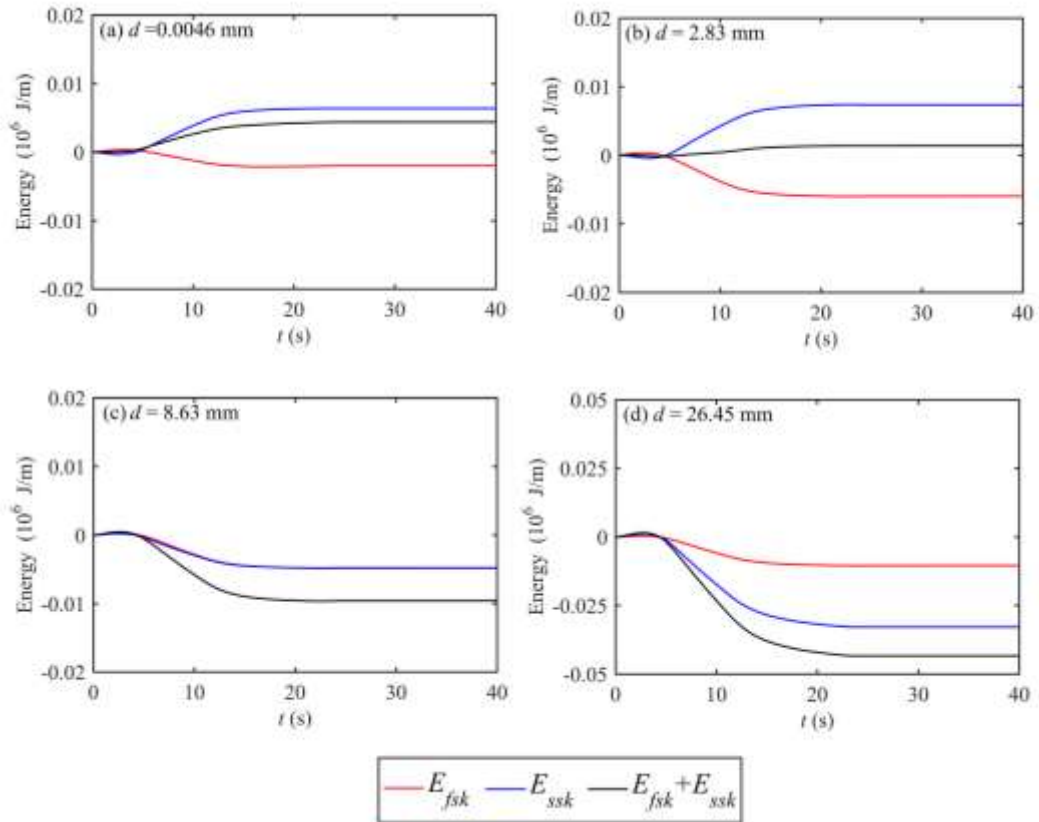
1128 exchange with the bed ( $E_{Gb}$ ), and energy dissipation due to bed resistance ( $E_R$ ) and

1129 fluctuation motions ( $E_D$ ) with the subscripts  $f$  and  $s$  denoting the liquid and solid

1130 phases, respectively. (b) Evolution of energy changes of the solid-liquid mixture ( $\Delta E$ ),

1131 solid phase ( $\Delta E_s$ ), and liquid phase ( $\Delta E_f$ ), and the work done by inter-phase ( $E_{fs}$

1132 and  $E_{sf}$ ) and inter-grain size interaction forces ( $E_{ss}$ ).



1133

1134

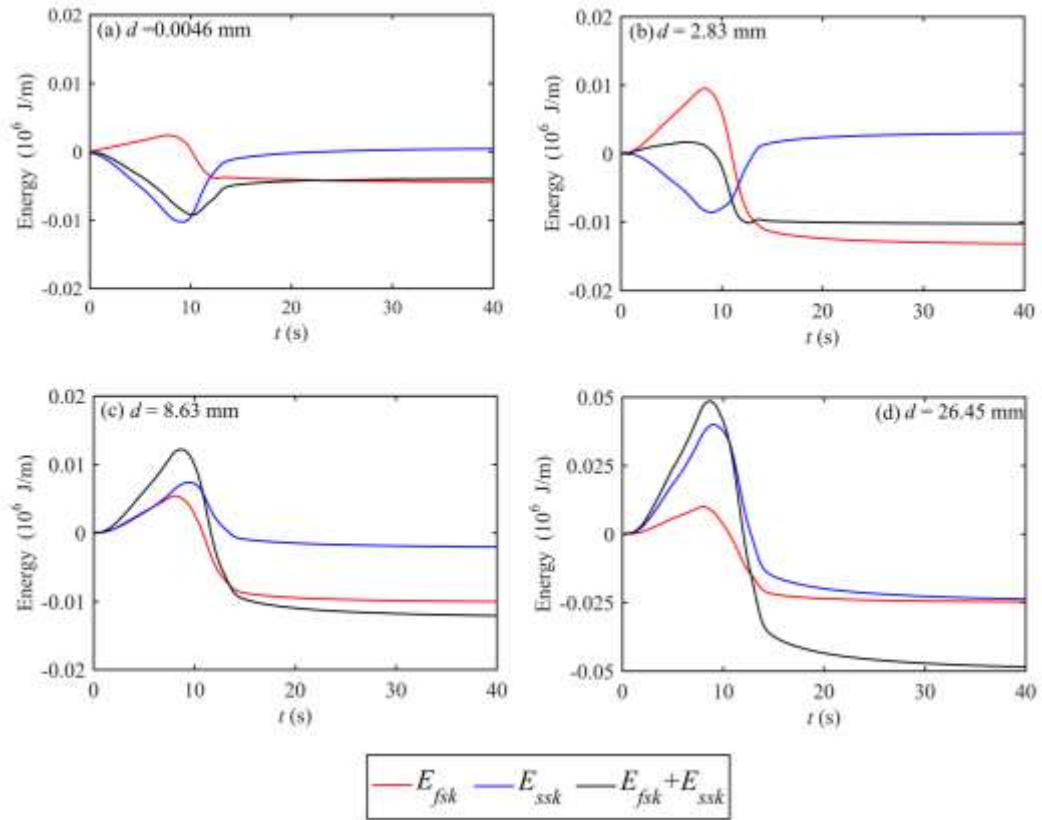
1135

1136

1137

1138

**FIGURE 7** Evolution of energy changes in size-specific grains for fixed-bed Case EXP-F. (a-b) fine grains; (c-d) coarse grains.  $E_{fsk}$  and  $E_{sfsk}$  represent work done by the inter-phase interaction force, and  $E_{ssk}$  represents work done by the inter-grain size interaction force.



1139

1140

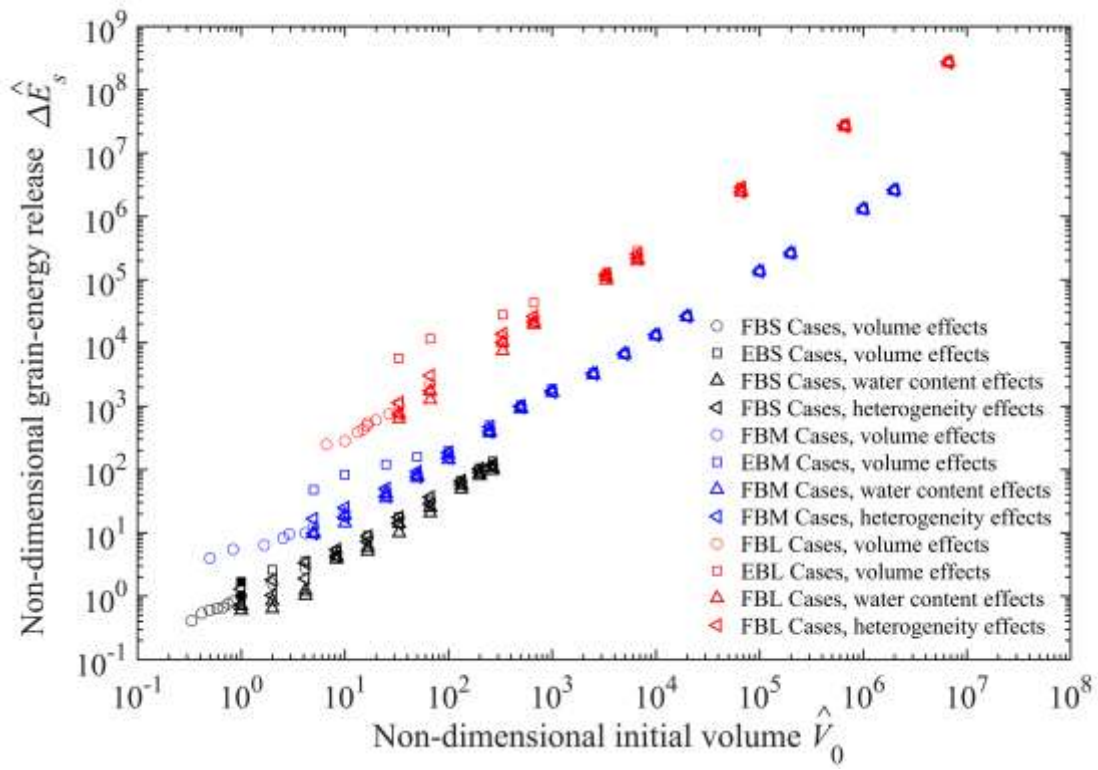
1141

1142

1143

1144

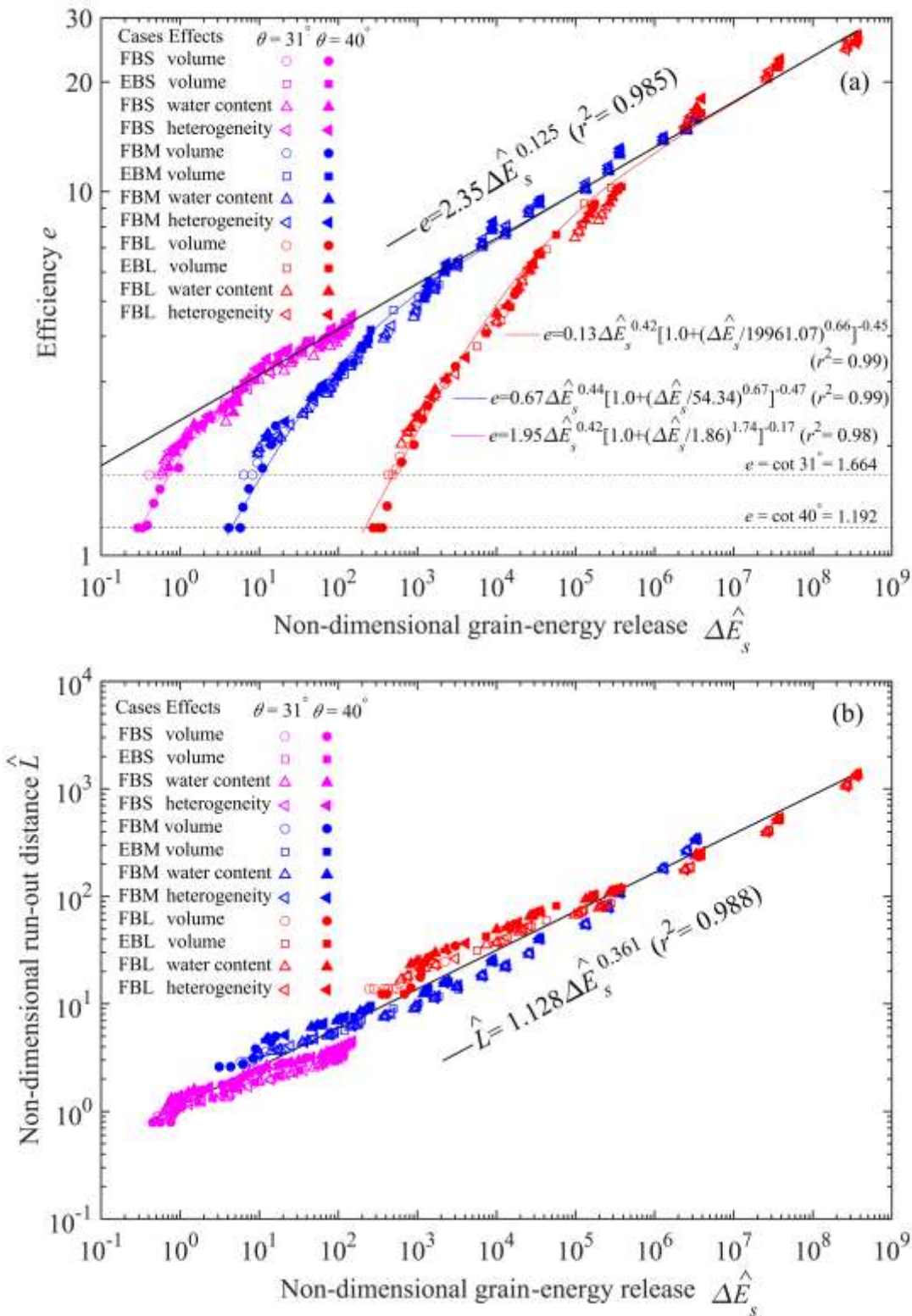
**FIGURE 8** Evolution of energy changes in size-specific grains for erodible-bed Case EXP-E. (a-b) fine grains; (c-d) coarse grains.  $E_{fsk}$  and  $E_{sfsk}$  represent work done by the inter-phase interaction force, and  $E_{ssk}$  represents work done by the inter-grain size interaction force.



1145

1146 **FIGURE 9** Dependence of non-dimensional grain-energy release  $\Delta\hat{E}_s$  on

1147 non-dimensional initial debris flow volume  $\hat{V}_0$  over a  $31^\circ$  sloping ramp.



1148

1149

**FIGURE 10** Debris flow mobility versus grain-energy release. (a) Dependence of

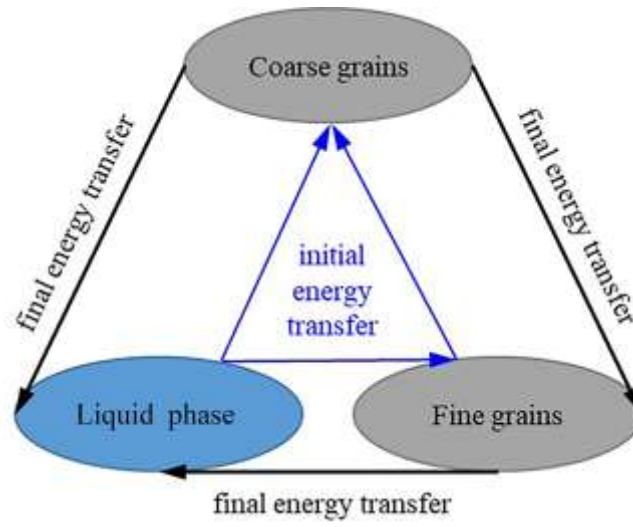
1150

efficiency  $e$  on non-dimensional grain-energy release  $\Delta \hat{E}_s$ ; (b) Dependence of

1151

non-dimensional run-out distance  $\hat{L}$  on non-dimensional grain-energy release  $\Delta \hat{E}_s$ .

1152



1153

1154 **FIGURE 11** Energy transfer between liquid, fine grains, and coarse grains in debris  
1155 flow.

1156